Coastal Engineering 199 (2025) 104748

Contents lists available at ScienceDirect

Coastal Engineering

journal homepage: www.elsevier.com/locate/coastaleng

# Seamless nearshore topo-bathymetry reconstruction from lidar scanners: A Proof-of-Concept based on a dedicated field experiment at Duck, NC

Kévin Martins [a,*], Katherine L. Brodie [b], Julia W. Fiedler [c,d], Annika M. O'Dea [b], Nicholas J. Spore [b], Robert L. Grenzeback [d], Patrick J. Dickhudt [b], Spicer Bak [b], Olivier de Viron [a], Philippe Bonneton [e]

[a] UMR 7266 LIENSs, CNRS – La Rochelle University, 2 rue Olympe de Gouges, 17000 La Rochelle, France
[b] Coastal and Hydraulics Laboratory, U.S. Army Engineer Research and Development Center, 1261 Duck Rd, Duck, 27949, NC, USA
[c] University of Hawai'i at Mānoa, Honolulu, HI, USA
[d] Scripps Institution of Oceanography, UC San Diego, La Jolla, CA, USA
[e] Univ. Bordeaux, CNRS, Bordeaux INP, EPOC, UMR 5805, F-33600 Pessac, France

ARTICLE INFO

*Keywords:*
Nearshore depth-inversion
Boussinesq theory
Surf zone
Lidar remote sensing

ABSTRACT

Accurate observations of the nearshore bathymetry, including within the breaking wave region, are critical for the prediction of coastal hazards, and improved understanding of sandy beach morphological response to storms. In this paper, we implement the recent Boussinesq theory-based depth inversion methodology of Martins et al. (*Geophys. Res. Lett.*, 50 (2023), Article e2022GL100498) to single- and multibeam lidar datasets collected during a dedicated field experiment on a sandy Atlantic Ocean beach near Duck, North Carolina. Compared with common approaches based on passive remote sensing technology (*e.g.*, optical imagery), lidar scanners present several key advantages, including the capacity to directly measure the beach topography, waveforms and the cross-shore variations in mean water levels due to wave action (*e.g.*, the wave setup), leading to the seamless reconstruction of a vertically-referenced beach topo-bathymetry. Given the potentially gappy nature of lidar data, particular attention is paid to the robust computation of surface elevation spectral and bispectral quantities, which are at the base of the proposed non-linear depth inversion methodology. Promising results on the final topo/bathymetry are obtained under contrasting wave conditions in terms of non-linearity and peak period, with an overall root-mean square error below 0.3 m obtained along a cross-shore transect covering both shoaling and breaking wave conditions. The accuracy of the final bathymetry in the shoaling and outer surf regions is generally found to be excellent, with similar skills as previously obtained in laboratory settings (relative error $< 10-15\%$). Under the most energetic conditions, an underestimation of the wave phase velocity spectra is observed within the surf zone with all theoretical frameworks, potentially owing to surf zone vortical motions not yet accounted for in the present methodology. This underestimation of the wave phase velocities results in a relatively large overestimation of the mean water depth, between 30% to 100% depending on the theoretical framework. With the methodology described herein, lidars bring new perspectives for seamlessly mapping the nearshore topo/bathymetry, and its temporal evolution across a wide range of scales. Although currently limited to a single cross-shore transect, we believe that opportunities exist to integrate multiple remote sensors, which could address individual sensor limitations, such as coverage (lidar) or the incapacity to directly measure waveforms (optical imagery).

## 1. Introduction

The coastal science community currently lacks insights into the rapid morphological evolution of sandy beaches during storms and extreme events (Sherwood et al., 2022). This knowledge gap is largely due to the challenge of measuring nearshore seabed elevation (bathymetry) with the necessary spatial and temporal resolution. Accurate bathymetric information, while critical for various oceanographic applications – such as navigation and coastal hazard prediction – remains difficult to obtain and track through time. Traditional methods, including shipborne sonars (*e.g.*, single or multibeam echo-sounders), offer centimeter-level resolution and accuracy but are constrained by

* Corresponding author.
*E-mail address:* kevin.martins@univ-lr.fr (K. Martins).

https://doi.org/10.1016/j.coastaleng.2025.104748
Received 29 January 2025; Received in revised form 16 March 2025; Accepted 17 March 2025
Available online 27 March 2025

limited spatial coverage, are time-consuming, and can be prohibitively costly, making them more suitable for localized areas such as harbours. Airborne lidar techniques, routinely employed to map coastal topo-bathymetry at larger scales ($O$(1–100 km)), take advantage of the relatively weak absorption of blue–green lasers in shallow, clear waters (*e.g.*, see Lyzenga, 1985; Irish and Lillycrop, 1999). Satellites equipped with multispectral sensors can operate at even larger spatial scales, from regional to global, albeit with lower resolution. In environments where water properties are well understood, these sensors can still provide reliable depth estimates (*e.g.*, see Stumpf et al., 2003; Salameh et al., 2019). However, none of these methods is well-suited for mapping the surf zone, where energetic wave breaking occurs, and even less at temporal scales relevant for studying the morphological response of beach systems to storms. This limitation stems from either safety concerns or technical challenges, such as lasers and optical signals being blocked by foam and sea spray in this highly dynamic region (Reineman et al., 2009; Vrbancich et al., 2011). Consequently, alternative approaches are needed to effectively map the bathymetry in wave-dominated coastal environments, and its evolution through time.

Along wave-dominated coastlines, remote-sensing technologies such as video cameras or X-band radars, combined with depth inversion algorithms based on ocean wave dynamics, have emerged as some of the most promising approaches explored over the last few decades. These solutions provide well-resolved information at scales relevant to nearshore processes in a cost-effective manner, while minimizing the risks associated with human intervention or equipment maintenance requirements (Holman and Haller, 2013). Depth inversion approaches rely on the strong relationship between nearshore wave dynamics and bathymetry, which allows remotely-sensed wave quantities to be linked with the mean water depth. The linear dispersion relation is the most commonly used theoretical framework, as it provides – when neglecting currents – a direct relationship between the water depth $h$ and the dispersive properties of a linear wave field:

$$\omega^2 = g\kappa_L \tanh(\kappa_L h), \tag{1}$$

where $\omega = 2\pi f$ is the angular wave frequency, $g$ is the acceleration of gravity and $\kappa_L$ refers to the (single-valued) magnitude of the wavenumber solution to the linear wave dispersion relation. Hereafter, $\kappa$ will denote the wavenumber magnitude, which, together with $\omega$, defines the wave phase speed $c(\omega) = \omega/\kappa(\omega)$. Early nearshore depth inversion algorithms used spectral analysis of video imagery to estimate pairs of $(\omega, \kappa(\omega))$ (Stockdon and Holman, 2000; Plant et al., 2008), from which the mean water depth can be inferred through Eq. (1). A vertically-referenced bathymetry is then retrieved using an estimate of the referenced mean sea-surface elevation at the time the depth was estimated (*e.g.*, from a nearby tide gauge). These efforts led to the development of *cBathy* (Holman et al., 2013), a community tool[1] under continuous development that has now been applied to environments characterized by a relatively wide range of tidal and wave conditions (*e.g.*, see Bergsma et al., 2016; Brodie et al., 2018; Bouvier et al., 2020; Rodríguez-Padilla et al., 2022; Lange et al., 2023). A number of other algorithms based on optical imagery exist for extracting pairs of frequency and wavenumbers, such as those based on wavelet transforms or empirical mode decomposition of the wave field (*e.g.*, see Simarro et al., 2019; Gawehn et al., 2021; Santos et al., 2022). Alternative approaches working in the time domain (*i.e.*, by evaluating a mean or bulk wave celerity) have also been proposed and tested (Lippmann and Holman, 1991; Catalán and Haller, 2008; Almar et al., 2008; Yoo et al., 2011; Matsuba and Sato, 2018; Kim et al., 2023b). As mentioned above, X-band marine radar products also offer the possibility of retrieving wavenumbers and frequency pairs, from which nearshore depths can be estimated with the linear wave dispersion (Honegger et al., 2019; Gawehn et al., 2020; Chernyshov et al., 2020). These approaches are similar in essence as they all depend on the linear wave dispersion relation to estimate depths from remotely-sensed wave dispersive properties, which are affected by modulation transfer functions (*i.e.*, waveforms are not directly measured).

In intermediate water depths, the linear dispersion relation (Eq. (1)) accurately describes the dispersive properties of low-amplitude wave fields, leading to typical errors in estimated water depth as low as 10% (*e.g.*, see Dugan et al., 2001; Holland, 2001; Brodie et al., 2018; Martins et al., 2023). However, in the shoaling region and closer to the breaking point, non-linear amplitude dispersion effects intensify, causing significant deviations of dominant wavenumbers from the predictions of the linear wave dispersion relation (Thornton and Guza, 1982; Elgar and Guza, 1985b; Herbers et al., 2002; Martins et al., 2021b). The overestimation of dominant wavenumbers by the linear dispersion relation in the nearshore leads to a consistent overestimation of inverted water depths in the shoaling region (*e.g.*, see Grilli, 1998; Brodie et al., 2018; Lange et al., 2023), with errors as high as 60 – 70% over prominent features such as sandbars (Bergsma and Almar, 2018; Martins et al., 2023). In the surf zone, non-linear amplitude dispersion effects dominate over frequency dispersion, leading to errors typically exceeding 40–50%, even when the accuracy of extracted phase speeds is carefully controlled or when those originate from direct wave measurements (Catalán and Haller, 2008; Fiedler et al., 2021; Martins et al., 2023). In this region, errors obtained using *cBathy* typically range within 50 – 600%, and generally increase with incoming wave energy (Holland, 2001; Bergsma et al., 2016; Brodie et al., 2018). The linear theoretical framework used for depth retrieval explains part of this error in this region where waves exhibit strongly non-linear behaviour; however, a significant portion of the error arises from uncertainties in the $(\omega, \kappa(\omega))$ observations. In the shoaling region, the impact of the modulation transfer function, which relates remotely-sensed wave properties to the actual waveform (*e.g.*, see Stockdon and Holman, 2000; Bergsma et al., 2019), has received limited attention but is believed to have minimal impact on the robustness of wavenumber estimates. This is not the case near the breaking point, where dark pixels associated with steep breaking waves rapidly switch to bright and white pixels, causing sudden shifts in extracted wave phases (Brodie et al., 2018; Bergsma et al., 2019). As such, not only do traditional depth inversion algorithms based on the linear theoretical framework have strong limitations in the nearshore region (Martins et al., 2023), but wave dispersive properties cannot be reliably estimated from traditional optical imagery, severely limiting our ability to retrieve depths in the wave breaking region.

To address these challenges, recent studies have explored the possibility of using machine learning techniques to improve the accuracy of depth estimates using wave synthetic observations (*e.g.*, see Collins et al., 2020) or proposed to combine both frequency-domain (such as *cBathy*) and temporal methods to estimate wave dispersive properties in regions where each approach is most effective – outside the surf zone and within it, respectively (Lange et al., 2023). However, depth inversion methodologies based on passive sensors inherently suffer from other critical limitations for the long-term objective of monitoring nearshore morphological changes during storms. These include the inability to operate at night, and the systematic neglect of wave setup, which varies significantly within the surf zone (*e.g.*, see Apotsos et al., 2007; Martins et al., 2022) and can reach 1 m near the coastline during storms (Fiedler et al., 2015; Nicolae-Lerma et al., 2017; Guérin et al., 2018).

In this work, we develop a methodology based on lidar technology to estimate the nearshore topo-bathymetry seamlessly, from the shoaling region to the subaerial section of the beach. This methodology is tested and presented as Proof-of-Concept on multi-source (ground-based and airborne) lidar data collected during a dedicated field campaign organized in September 2022 at Duck, NC, USA. Over the past decade, lidar remote sensing technology has demonstrated its capability to continuously monitor the morphological evolution

[1] https://github.com/Coastal-Imaging-Research-Network/cBathy-Toolbox

of subaerial sections of beaches across temporal scales ranging from individual swash events (Vousdoukas et al., 2014; Bayle et al., 2023; Blenkinsopp et al., 2024), to storms (Brodie et al., 2012; Almeida et al., 2015; Martins et al., 2016; Kim et al., 2023a) and seasons (Phillips et al., 2019; O'Dea and Brodie, 2024). In contrast with approaches based on optical imagery and marine radars, lidars also offer the significant advantage of directly measuring free surface elevation, providing high-resolution information on waveforms across the shoaling and breaking wave regions (Irish et al., 2006; Blenkinsopp et al., 2010, 2012; Brodie et al., 2015; Martins et al., 2017a; Fiedler et al., 2021; O'Dea et al., 2021a). Because lidar scanners are not affected by the modulation transfer function issue and inherently capture non-linear wave dynamics, they present a highly promising remote sensing technology for robustly estimating nearshore topo-bathymetry, even within the challenging surf zone.

The framework we develop here builds upon Martins et al. (2023), who proposed a novel non-linear (Boussinesq-based) bathymetry-inversion methodology adapted to highly-resolved maps of free surface elevation measurements. Given that it relies on spectral and bispectral estimates of free surface measurements, a significant portion of this article focuses on adapting an approach originally designed and tested on continuous wave gauge data to accommodate gappy data collected by multibeam lidars mounted on nearly-stationary airborne platforms (uncrewed aircraft systems, UAS). This adaptation is crucial for extending the applicability of the method to more dynamic and flexible data collection scenarios. A Monte Carlo-like methodology is also introduced for estimating statistical uncertainties on depth estimates. By addressing these challenges, we aim to demonstrate the robustness and versatility of the adapted methodology, paving the way for more reliable bathymetric estimates in the nearshore region, including the surf zone.

## 2. Field site and the BELS 2022 campaign

The "nearshore Bathymetry Estimate from Lidar Scanners" (BELS) field campaign was organized from 12 to 25 of September 2022 along a sandy beach facing the Atlantic Ocean near Duck, North Carolina, USA at the U.S. Army Engineer Research and Development Centre's Field Research Facility (FRF). The FRF is one of the most well-studied coastal research sites in the world, and the comprehensive datasets of nearshore hydrodynamics and sediment transport collected at this site over the last four decades contributed to significantly advancing our understanding of nearshore dynamics. The objectives of the BELS field campaign were to adapt, apply, and assess the new non-linear (Boussinesq-based) depth inversion method of Martins et al. (2023) on real-world lidar datasets. Our efforts concentrated along the beach cross-shore transect located on the northern side of the pier at the approximate FRF longshore coordinate $y = 945$ m, where a fixed line-scanning lidar is stationed on the dune crest (O'Dea et al., 2019). An overview of the 3D topo-bathymetry surveyed 2 weeks before the start of the experiments is displayed in Fig. 1, along with the experimental setup that is described next. The spatial data are presented in the FRF local coordinate system with cross- ('x') and alongshore ('y') axes, centred at 36.1776° N, 75.7497° W, respectively, and rotated 17.8° from true North.

### 2.1. Beach and free surface elevation lidar measurements

A total of three lidar systems, line-scanning and multibeam, were used to synchronously collect free surface elevation data across the shoaling, surf and swash zones. The line-scanning dune lidar (Riegl VZ-1000, 1550 nm laser with a 0.3 mrad beam width) continuously scans for 30 min every hour along the cross-shore transect near $y = 945$ m, and uses a co-registration procedure to transform lidar measurements of beach and free surface elevation into real-world coordinates (Brodie et al., 2015; O'Dea et al., 2019). Due to the presence of a low-tide terrace extending to $x \sim 180$ m during the experiments (see Fig. 1b), lidar returns were nearly continuous (*i.e.* without data gaps) up to this location for moderate energy conditions (significant wave height $H_{m0} > 1$ m). This line-scanning lidar was complemented by datasets collected by two multi-beam lidars mounted on multirotor small UASs, following the strategy of Fiedler et al. (2021) and Feddersen et al. (2024). Both the FRF and Scripps Institute of Oceanography (SIO) teams participating in these experiments possessed an autonomous system, referred to in the following as the FRF and SIO UAS lidars. The SIO UAS payload was a Phoenix Lidar Systems (PLS) miniRANGER LITE, consisting of a Velodyne VLP–32C on the 12–13 of September, and a line-scanning Riegl miniVUX–1UAV lidar on the 14 of September (no SIO flights after this date). The FRF UAS payload was a Phoenix Lidar Systems (PLS) miniRANGER LITE, consisting of a Velodyne HDL–32E. Both FRF and SIO multibeam lidars emit 32 beams of 905 nm wavelength, but their specifications (precision, range, vertical resolution and field of view etc.) slightly vary so that the interested reader is invited to read the detailed manuals provided by the constructor. Below, the lidars differences and specificities will only be described qualitatively and raw data points are all processed in a similar fashion.

### 2.2. Beach topography and bathymetry surveys/monitoring

Topographic and bathymetric surveys around the FRF pier are regularly performed using a combination of amphibious vehicles/vessels such as the Coastal Research Amphibious Buggy (CRAB). During comprehensive experiments like BELS, the frequency of these surveys can increase and they can be performed almost on a daily basis. Each day UAS flights were performed, the topo-bathymetry was surveyed by the CRAB at least until the last cross-shore position sensed by the multibeam lidars. Though performed daily, these surveys have practical limitations due to the size and wheels configuration of the CRAB: the minimal longshore distance of surveyed transects to the instrumented one is typically greater than 20 m and uncertainties exist on the vertical accuracy to describe bedforms with wavelengths smaller than a few meters. For this reason, surveys were complemented by an Amphibious Uncrewed Ground Vehicle (hereafter the 'crawler'), which provided highly-detailed cross-shore topo-bathymetric surveys in a flexible manner but only under low-energy wave conditions (Bak et al., 2023). At fixed locations in the shoaling and breaking wave regions (numbered #1 – 5, positions ranging $x = 130 - 180$ m), five full backscatter ultrasonic altimeters (Echologger EA400) were deployed on the 16 of September to capture rapid morphological changes. The altimeters were mounted to heavy, 0.08 m diameter, round pipes jetted a couple of meters into the seafloor from the CRAB. Except for #5, the elevation of the altimeters relative to NAVD88 was determined at low tide with RTK-GPS using corrections from a local base station. At altimeter #5, the elevation was indirectly retrieved from the co-located pressure sensor, whose position relative to the altimeter was known within a cm accuracy, by matching with the mean water levels measured at the pier under low energy conditions (negligible setup/setdown). Outside of the breaking region and under low to moderate energy conditions, the seabed elevation was estimated from bottom-finding algorithms using vertical profiles of acoustic backscatter (Brodie et al., 2018). Under breaking conditions, the backscatter intensity was too intense for these algorithms to work robustly. Instead, the seabed elevation was retrieved manually from timestacks of backscatter variances, which remains low and stable right under the seabed layer in contrast with the bottom of the water column.

### 2.3. In situ water levels and wave measurements

Mean water level data were continuously collected at the pier while a permanent array of pressure sensors deployed in 8 m-depth continuously provided estimates of the directional wave forcing in intermediate water depth (hereafter the 8 m array; see Long, 1996,

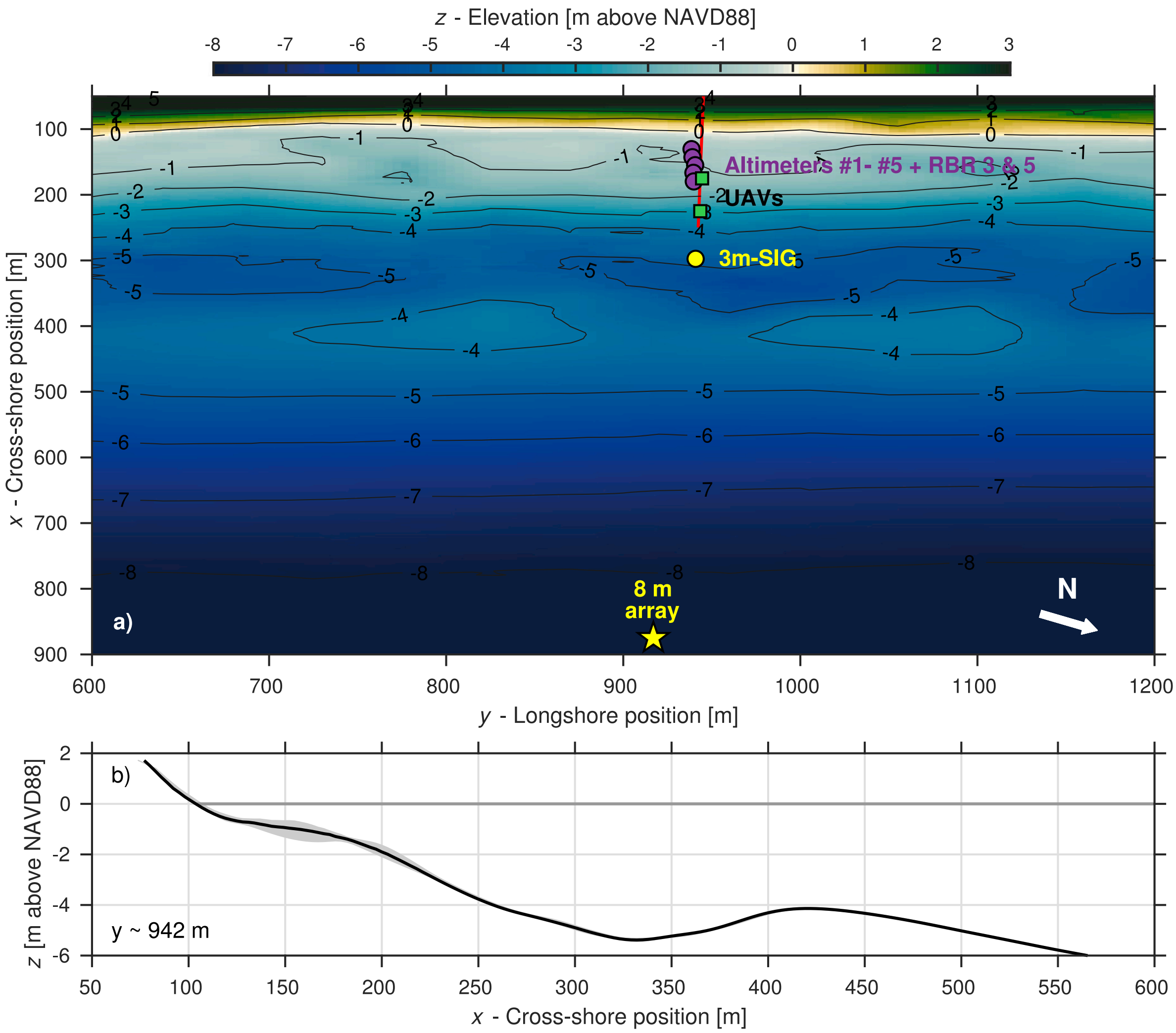


**Fig. 1.** Topography and bathymetry map of the sandy beach at the FRF (Duck, NC, USA) surveyed on the 22 of August 2022. The top panel (a) shows contour maps as well as an overview of the experimental setup, while the bottom panel (b) shows the cross-shore evolution of the beach profile around the instrumented transect. The grey-shaded area shows the envelope of bathymetric changes between 12 and 27 September 2022, providing insights on the morphological changes during the experiments. The coastline faces the Atlantic Ocean with an orientation of 71.2° with respect to the North. Spatial coordinates are displayed in the FRF coordinate system ($x$: cross-shore coordinate; $y$: longshore coordinate) while the vertical elevation is given relative to the North American Vertical Datum of 1988 (NAVD 88). The red line corresponds to the line scanned by the dune lidar system. Altimeters #1 – #5 (violet points) were deployed approximately 12.5 m apart between $x = 130 - 180$ m along a transect around $y \sim 940$ m to minimize the risks of obstruction for the dune lidar. Two pressure sensors were bottom-mounted at the locations of altimeters #3 and #5. The green squares correspond to the two UAS multibeam lidar averaged hovering positions ($x = 175$ and 225 m) while the yellow symbols show the location of the permanent sensors, including the 8 m pressure array from which the offshore wave forcing is estimated (Long, 1996).

for more details). Other permanent sensors at the FRF include the Nortek Signature1000 deployed in 3 m water depth (3m-SIG), which provides a good indication of the incident wave forcing at the most seaward location sensed by the lidars ($x \sim 250$ m). Bulk wave properties estimated from linear wave theory at the 8 m array and at 3 m-SIG are shown in Fig. 2. Two additional $\text{RBR}_{\text{solo}}$ pressure sensors were deployed near the seabed at the cross-shore location of altimeters #3 ($x = 155$ m) and #5 ($x = 180$ m). The data from these sensors is mostly used here to assess the accuracy of UAS lidar-derived wavenumber estimates and quantify vertical biases in the UAS lidar datasets. The free surface elevation was recovered from raw pressure signals corrected for atmospheric pressure measured at the pier using the moderately dispersive non-linear reconstruction method proposed by Martins et al. (2021a). This reconstruction uses the Boussinesq theory of Herbers et al. (2002) to estimate non-linear frequency and amplitude dispersion effects on wavenumbers. More details on this Boussinesq theory are given below, in Section 4.1, as the non-linear depth inversion methodology of Martins et al. (2023) is based upon it.

### 2.4. Tidal and wave conditions during UAS flights

A total of 21 flights were performed during the BELS experiments, as weather and wind conditions allowed (Fig. 2a). Except for the first flight of 13 September (flight #3, 14:00–14:30 UTC), during which only the SIO UAS flew with a hovering cross-shore position at $x = 175$ m, the approximate hovering positions of the FRF and SIO UAS were $x = 175$ m and $x = 225$ m, respectively. During these 21 flights, a relatively wide range of tidal and wave conditions were covered, as illustrated in Fig. 2. The best datasets were collected over the first three days of the experiments (12–14 of September) during which the dune lidar and the two UAS lidars synchronously collected data. For these three days, the tidal range varied within 1–1.3 m and incoming waves corresponded to nearly shore-normal propagating swell (incidence angle in 3 m-depth $< 10°$ relative to shore, see Fig. 2d), with significant wave height and wave peak period decreasing from 1.5 m and 16 s on the 12$^{\text{th}}$, respectively, to around 0.8 m and 12 s on the 14$^{\text{th}}$, respectively (Fig. 2bc). These conditions were followed by 5 to 6 very calm days, during which no flights were undertaken since the

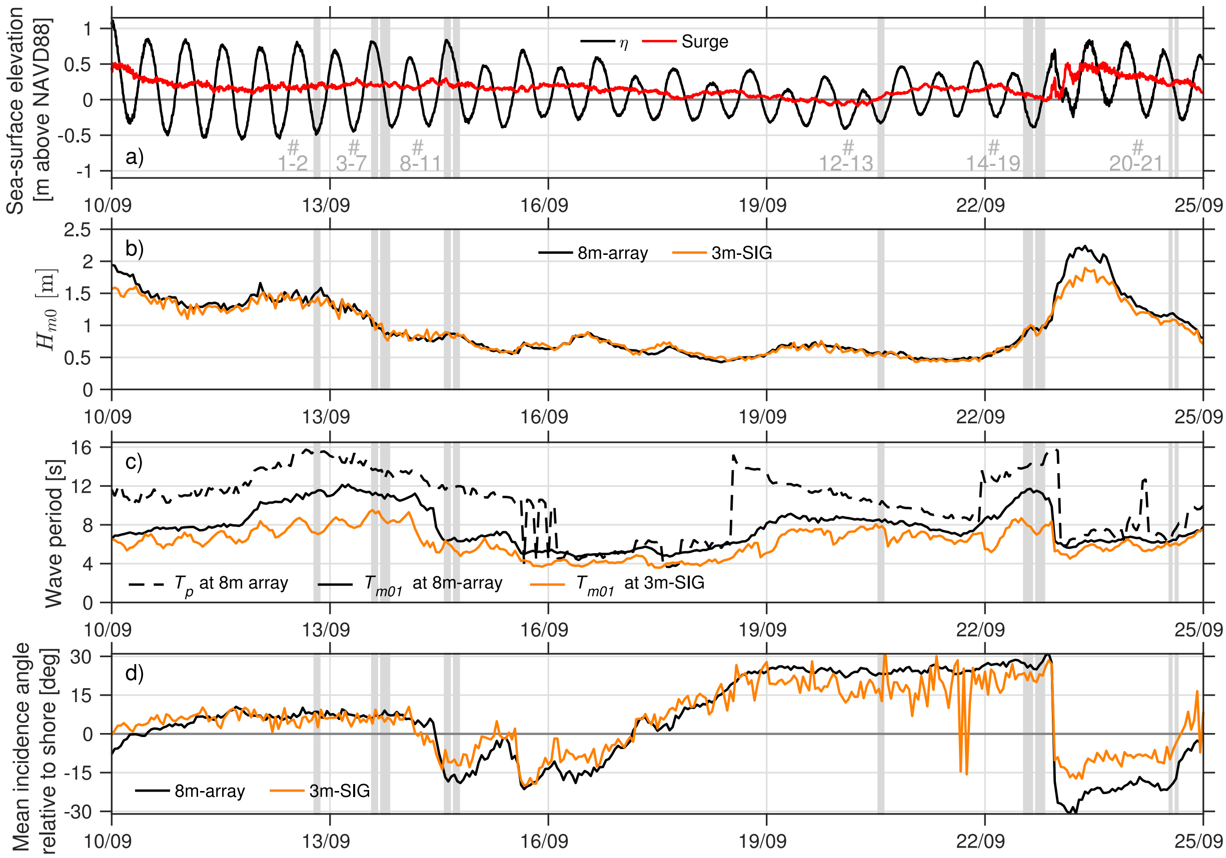


**Fig. 2.** Water levels and incident wave conditions during the BELS experiments (12–25 September 2022). Panel (a) shows the mean water surface elevation $\eta$ measured at the pier (NOAA station 8651370), with the corresponding surge anomaly. Lower panels display the wave conditions estimated at the 8 m array and at the 3 m-SIG (2.7 m mean water depth), including: the significant wave height $H_{m0}$ (b), the peak $T_p$ and mean $T_{m01}$ wave periods (c) and the mean wave direction relative to the mean shoreline orientation (d). In all panels, time windows where UAS flights were performed are indicated by the grey-shaded regions while the corresponding number, used throughout the manuscript, is indicated in panel a.

very narrow surf zone did not present much interest compared to the conditions experienced on the first days of the experiments. Two flights were performed with the UAS FRF during very mild conditions on the 20 of September. Conditions were more energetic during flights #14– 19 on the 22 of September, just prior to the 22–23 September Nor'easter, but incident waves propagated towards shore with a large incident angle (20–25° relative to shore, see Fig. 2d). Under such conditions, an estimation of the mean wave angle throughout the surf zone is required for accurately estimating the bathymetry. As no theoretical or practical frameworks currently exist for estimating surf zone waves mean angles from free surface elevation datasets only, these flights were not considered for the depth inversion. Finally, the conditions found during the two last flights performed with the FRF UAS on the 24 of September were particularly useful to cross-compare wavenumbers derived from the Boussinesq theory of Herbers et al. (2002) from both lidar and *in situ* pressure sensors that were deployed together with the altimeters.

## 3. Single and multibeam lidar data processing

### *3.1. A step-by-step procedure for merging and gridding multiple lidar data sources*

During flights #1 to #11 (12–14 of September 2022, see Fig. 2), up to three independent lidar systems (dune, FRF & SIO) were synchronously collecting upper beach topography and free surface elevation data over the swash, surf and shoaling zones. As the depth inversion approach of Martins et al. (2023) relies on time-gridded surface elevation data at fixed location in space (any sub-wavelength spacing), an important step concerns the interpolation of raw lidar point clouds into spatial and temporal interpolation grids. One possible approach is to process each individual dataset in an independent manner, perform the depth inversion on each dataset, and merge the individual bathymetry estimates into a final product. A potentially more straightforward approach, followed here, is to work on a single surface elevation dataset (as in Martins et al., 2017b). As it will be shown later in this section, merging the raw lidar datasets instead of the individual derived bathymetry actually presents several advantages in terms of the final product's accuracy. Though in principle the lidar systems work similarly (near infrared beams measuring a distance with the time-of-flight technique), each lidar system used here displayed specific characteristics that made the merging of their point cloud data a challenging task. This includes: a common GPS clock but different positioning systems and lidar firing times, line-scanning versus multi-beam lidars, rotation rates that affect the effective sampling frequency, varying spatial resolutions and accuracy, different points of view and hence surface slope detected etc. This is illustrated in Fig. 3 with an instantaneous snapshot of the lidar point clouds around 19:23:16 UTC on the 12 of September 2022. Fig. 3a shows the entire lidar coverage on the *xy* horizontal plane, while Fig. 3b displays the dune lidar data and UAS lidar points found within $y = 944.5 - 945$ m (0.5 m-wide longshore swath) on the *xz* vertical plane.

The UAS hovering positions were chosen to maximize lidar coverage and capture wave transformation processes over a region as wide as possible, ideally covering shoaling, near-breaking, and breaking waves, eventually propagating into the swash zone, as shown in Fig. 3. During flight #1 on the 12 of September (19:00–19:30 UTC, low-tide), the mean breaking point was located around $x$ = 200–210 m. Seaward

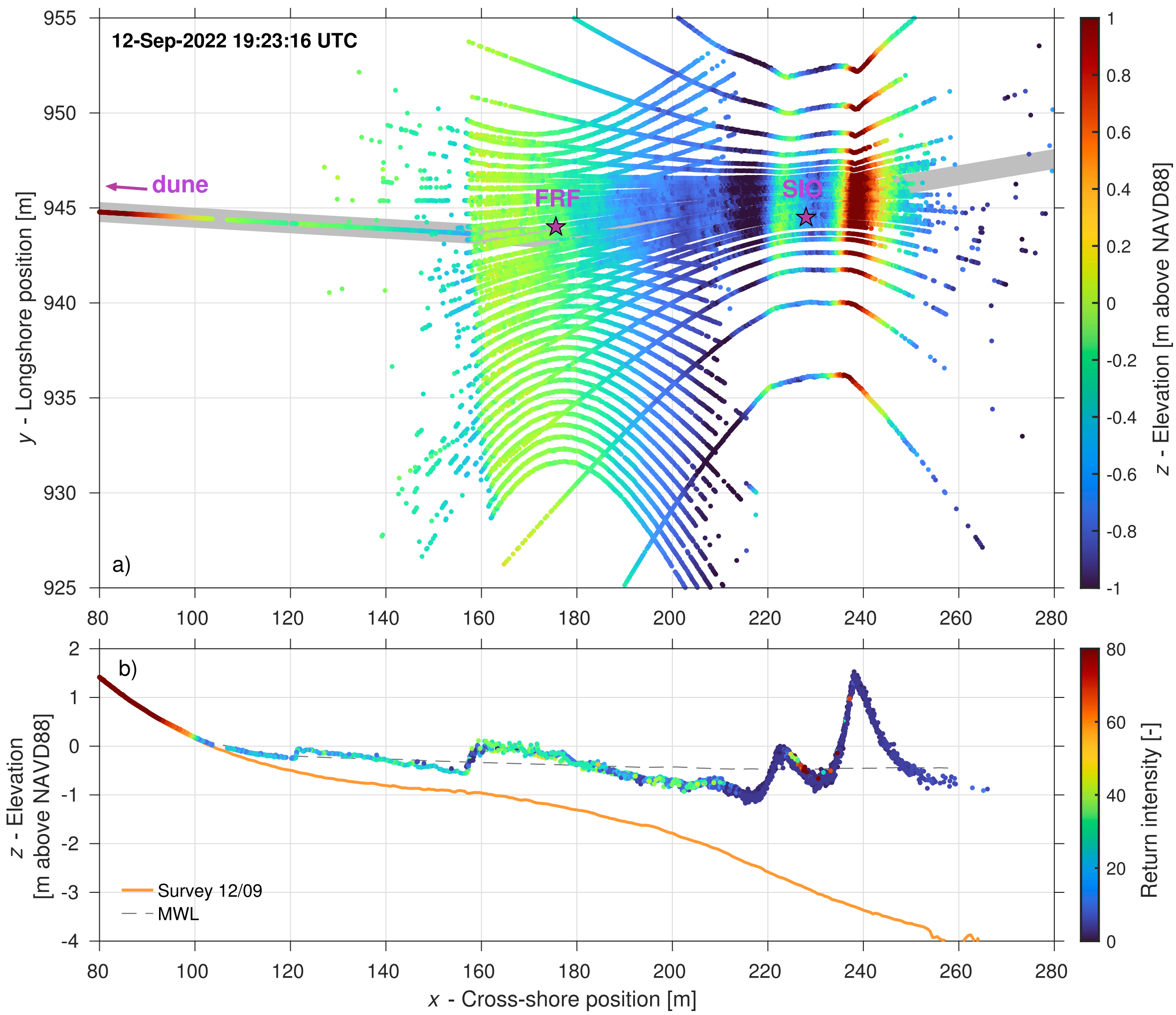


**Fig. 3.** An example lidar scan from the three independent systems around 19:23:16 UTC on the 12 of September 2022 (flight #1, 19:00–19:30 UTC). In panel (a), the raw lidar points are shown in alongshore versus cross-shore coordinates ($xy$ horizontal plane in the FRF coordinate system) and coloured by the vertical elevation relative to NAVD88. The two UAS hovering positions are indicated with the violet stars while the grey-shaded area indicates the modified "cross-shore" transect used for the depth inversion for this specific flight (see Step 2 in Section 3.1). Panel (b) shows the same data on the $xz$ vertical plane and coloured for return intensity along the topo-bathymetric profile and the lidar-derived mean water levels (MWL). In panel (b), only data points found within $y = 944.5 - 945$ m are shown.

of this point, shoaling and steepening near-breaking waves were successfully observed with the Velodyne VLP–32C (SIO lidar), the only lidar sensor here able to consistently detect the free surface elevation in the absence of remnant foam. In this area, returns intensity were generally low ($< 10$, see Fig. 3b), which is typical of very diffusive surfaces, except near nadir ($x \sim 228$ m) where they can reach 100. These values indicate that in this case, the water surface acts as a retro-reflector (Velodyne manual). On the contrary, the Velodyne HDL–32E (FRF lidar) performed well only with large quantities of foam generated during breaking. This can be seen from the clear demarcation line around $x \sim 210$ m from which no lidar returns are found seaward (Fig. 3b), in contrast with the relatively high-intensity returns associated with broken waves shoreward to this location. For the swell observed on that day, the Mean Water Level (MWL) measured by the array of lidars and shown in Fig. 3b also helps to identify the transition between these nearshore regions where waves exhibit contrasting wave shapes. Prior to breaking ($x \sim 220$–240 m), incident waves display a strong horizontal asymmetry (skewness), the MWL sitting nearly at trough levels. In contrast, asymmetry relative to the vertical axis largely dominates in the inner surf zone, where broken waves clearly exhibited a saw-tooth shape (Fig. 3b). This is consistent with past observations made both in the field (*e.g.*, Elgar and Guza, 1985a) or in laboratory conditions (Martins et al., 2021b).

In order to merge the lidar datasets and grid them for further analysis, we implemented the following procedure:

**Step 1 —** *Lidar point clouds geo-rectification.* At the very least, all lidar data must be expressed within the same geo-referential system. For the dune lidar system, this is done as part of a standard processing procedure (O'Dea et al., 2019), where the horizontal coordinates are expressed in the FRF coordinate system, and the vertical measurements are referenced to the North American Vertical Datum of 1988 (NAVD 88). For the UAS lidars, GNSS trajectory data were post-processed and corrected to centimeter-level accuracy using an on-site National Geodetic Survey's (NGS) Continuously Operating Reference Station (CORS station NCDU) with the lidar integration software. Using these post-processed trajectories, raw laser data were then georectified into state plane coordinates (NAD83(2011), North Carolina State Plane, meters). Finally, the output was transformed into the local FRF coordinates. For further processing workflows, the reader is referred to Fiedler et al. (2021), Feddersen et al. (2024).

**Step 2 —** *Definition of a cross-shore transect.* As shown in Fig. 3a, the line scanned by the dune lidar is not perfectly aligned with the cross-shore axis of the FRF coordinate system. Since the theoretical hovering positions of the UAS lidars were determined assuming a perfectly cross-shore transect, this resulted in a mismatch between the dune lidar's scanning line and the highest UAS data point density (Fig. 3a). To account for this, a small angle ($\leq 2°$) was introduced at the point where the quality of the dune lidar signal began to degrade. For each flight, this angle was optimized to ensure that the modified transect passed directly beneath the UAS positions. Given the small magnitude of the angle, its effect on the estimation of cross-shore wave propagation speed from gridded lidar data is negligible ($< 0.1\%$ error). While bathymetric data will be computed at 1-meter intervals, a cross-shore spacing of 0.2 meters is applied between points along this modified transect for the free surface elevation interpolation.

**Step 3 —** *Homogenizing lidar vertical offsets*. As analysed below in Section 3.2, the three lidar systems showed slight differences in their mean vertical elevations. Although the dune lidar system uses an advanced co-registration algorithm for each of the 30-min data collection (O'Dea et al., 2019), it may still develop vertical biases several hundred meters away from the scanner due to small uncertainties on the retrieved rotation matrix. The UAS lidars, measuring much closer to nadir, primarily experience vertical bias due to GPS errors, typically within a few centimeters. Here, the dune lidar system is treated as unbiased, meaning that it is assumed to collect data relative to a fixed vertical datum and the two UAS lidars were corrected to match it. We first corrected the bias within the FRF dataset by comparing differences in mean elevations with the dune lidar for each hover (up to 3 hovers per flight). This comparison was done by comparing individually-gridded versions of the two surface elevation datasets at the cross-shore location with the most overlapping returns. Once the bias was computed, it was considered spatially uniform but time-varying with a 2-min moving average, and corrected for on all FRF lidar points. The same process was then repeated for the SIO lidar point cloud, by comparing it with the corrected FRF dataset. As it will be shown, the vertical differences in mean elevations computed from the different lidar sources never exceeded 8 cm for all 21 flights, demonstrating the accuracy and robustness of all systems.

**Step 4 —** *Spatial and temporal gridding.* The interpolation process starts by selecting a temporal grid $T_i$ and a spatial resolution $\delta x$. Except when specified otherwise, all spectral results described in this manuscript, including bathymetry inversion, were obtained with a sampling frequency of 2 Hz and a spatial resolution of $\delta x = 0.2$ m. For each point $t_i$ of $T_i$, a 4-D ($t$, $x$, $y$ and $z$) linear interpolant is generated using the equivalent of three full UAS lidar scans. Thus, for each interpolation at $t_i$, the algorithm searches for all data point collected at times within 0.16 s of $t_i$. Using more lidar full scans to create the interpolant (10 or 20 tested here) resulted in a slight smoothing of the largest surface elevation gradients. It is worth noting that the corresponding decrease of energy levels, which increased with the time interval chosen, only affected the tail region ($f \gtrsim 1$ Hz). As these frequencies are not considered in the depth inversion procedure (described in Section 4), this choice has no impact in the final results here. The algorithm then iterates over the cross-shore grid and performs the interpolation only when sufficient data points in the original point cloud are available around that location (typically a minimum of 4 points within a 1-m radius). Combined, these two steps – first in time then space – ensure quality control and prevent the artificial filling of large spatio-temporal gaps.

Below, datasets from individual lidar sources are also used in order to assess the accuracy of our data curation and processing strategy. For those, the same interpolation grids (Step 2) and methodology (Step 4) were used to ensure consistency between all datasets.

### 3.2. Accuracy of the lidar systems and the gridding procedure

The advantage of merging the raw lidar datasets prior to gridding them is illustrated in Fig. 4b with the cross-shore variations of the percentage of returns on individual and merged gridded datasets. Fig. 4a shows the corresponding profiles of significant wave height along with water levels. For this specific flight (#1 on 12 September, 19:00–19:30 UTC), three hovers were performed with the FRF UAS lidar system while only two were performed with the SIO UAS. Time intervals between hovers were used to perform figure-eights in order to restabilize the IMU, explaining the reduced amount of data for both UAS lidar systems compared to the continuous acquisition from the dune lidar. It is worth noting that on the 24 of September (flights #20 and #21), complete 30 min-long flights were performed without affecting the drone horizontal stability or deteriorating the lidar vertical accuracy as compared with flights split in several hovers (Fig. 5ab). Thus, we now believe that splitting the flights in several hovers is unnecessary for the present application. Besides facilitating the depth inversion procedure, Fig. 4b shows that merging the lidars prior to gridding them results in overall more data being conserved. This is explained by the increased number of raw data points at a given location, thus overcoming potential filters based on the density of points cloud (see previous section), but also simply because of shadowing effects that are filled in by other lidars with different view angles. This is especially true around breaking, here typically between $x = 180$–$220$ m (Fig. 4b).

The accuracy of the lidar system is here first evaluated in terms of the UAS horizontal stability and lidar-derived mean water (vertical) elevation. Fig. 5a shows the variance of the detrended horizontal displacements measured by the Inertial Motion Unit (IMU) of the two UAS systems (FRF and SIO) for each flight. Note that the figure also provides an indication of which lidar package and when it was measuring during the flights. In terms of horizontal stability, the SIO UAS was surprisingly stable, with a displacement standard deviation $\sigma_{xy}$ an order of magnitude lower than that of the FRF UAS. Wind gusts, displayed in Fig. 5c, did not seem to play a major role in the horizontal stability of the UAS as there is no clear trend between weakening wind gusts and increased stability. The accuracy in the vertical is analysed by comparing the differences between the UAS lidar-derived mean sea-surface elevations to that measured by the dune lidar system. This comparison is shown in Fig. 5b, where multiple points for a single flight correspond to the different hovers (*i.e.*, one point per hover). Though of different horizontal stability, the two UAS lidars appear extremely stable in the vertical, with consistency throughout all flights. The differences in mean $z$ elevation relative to the dune lidar-derived values are of the order of the GPS accuracy, demonstrating the robustness of the UAS lidar systems. Differences between mean sea-surface elevations measured by the RBR#3 relative to the dune lidar are also shown in Fig. 5b. Interestingly, the vertical bias relative to the dune lidar system associated with the FRF lidar and RBR#3 display a very similar trend, with an excellent match and decreasing bias relative to the dune data for flights #12 to #15, and then later stabilizing with minor differences. This suggests that some of the relative differences shown here are actually inherited from the dune lidar co-registration procedure (O'Dea et al., 2019). Indeed, even very small errors in terms of optimal rotation matrix represent uncertainties of the order of several centimeters hundreds of meters away from the lidar. In the present case, this uncertainty is of the order of the GPS error and typically less than a few centimeters. While uncertainties associated with the GPS positioning of the UAS do not affect the lidar-inverted depth, it does impact the final bathymetry since it is retrieved

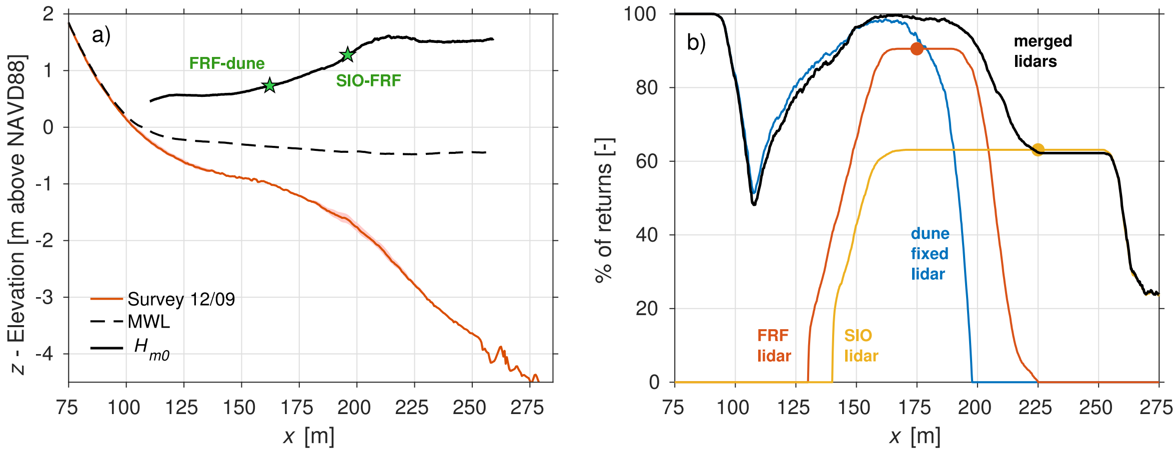


**Fig. 4.** Overview on the quality of individual and merged gridded lidar datasets during flight #1 on 12 September 2022 (19:00–19:30 UTC). Panel (a) shows the cross-shore evolution of the significant wave height along with mean water levels (data points with less than 50% returns in the series were removed). Panel (b) shows the percentage of returns for each individual dataset (dune, UAS FRF and SIO) and merged gridded dataset at 2 Hz.

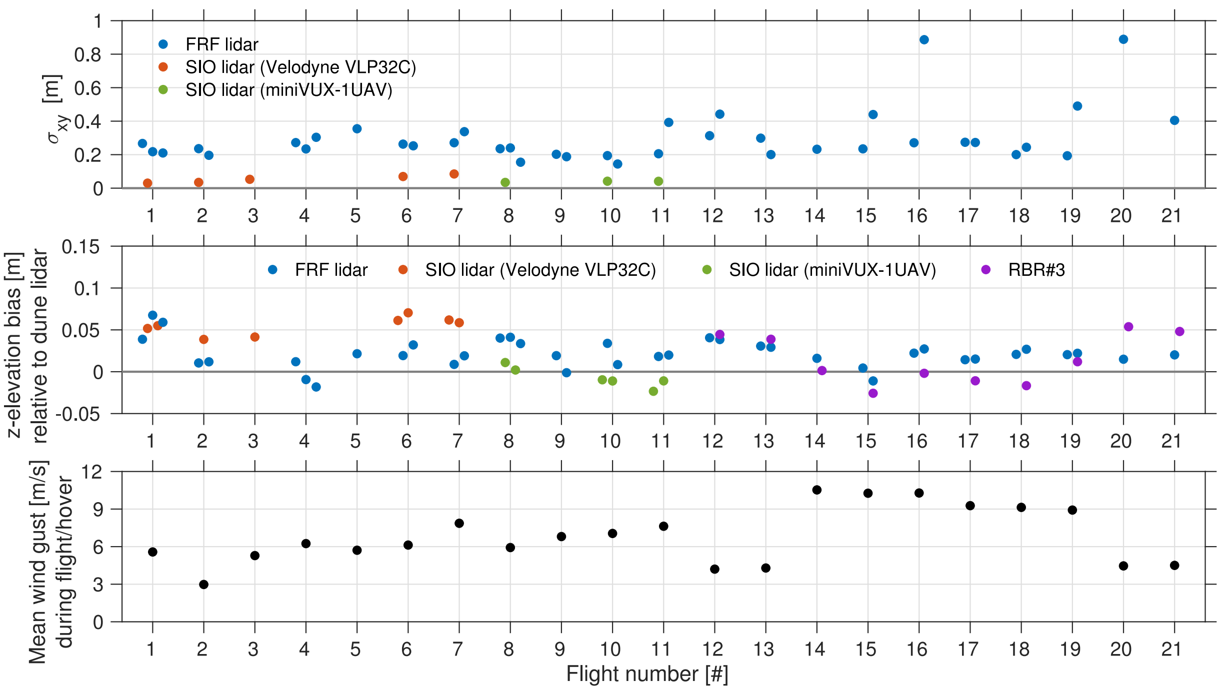


**Fig. 5.** Panel (a) shows the horizontal stability of the two UAS systems (FRF & SIO), assessed through the standard deviation of its horizontal position during each hover (*i.e.*, variations relative to its mean position. Panel (b) compares the differences in mean sea-surface elevation measured by the UAS lidars relative to the dune lidar. For flights performed after 16 September 2022, on which the sensor was deployed, data points from the RBR#3 are also shown. Panel (c) shows the mean wind gusts measured at approximately 19 m above MSL during the corresponding flight. Wind gusts are defined as the highest 5 s average velocities, as in the meteorological products from the FRF (see Acknowledgements for further details on data access).

by subtracting the inverted depth from the lidar-derived mean sea-surface elevation. An uncertainty of around 5–6 cm on the UAS vertical positioning, as obtained here (Fig. 5), is found acceptable in the present situation given the desired accuracy of the depth inversion system and that of the surveys used for the method's assessment (the CRAB, surveying 20+ m either side of the monitored transect).

A more thorough evaluation of the lidar-derived timeseries of free surface elevation $\zeta$ (detrended sea-surface elevation) was also performed through spectral and cross-spectral analyses (see Appendix for details). In Fig. 6ab, we compare the energy spectra of individually-gridded lidar datasets at two contrasting locations annotated by the green stars in Fig. 4a: in the inner surf zone (dune vs. FRF, panel a) and in the outer surf zone (FRF vs. SIO, panel b). For each location, the energy spectra of the free surface elevation difference timeseries is also shown. In terms of energy density, an excellent match is found between the FRF and dune lidar datasets in the inner surf zone (Fig. 6a) and between the FRF and SIO lidar datasets in the outer surf zone (Fig. 6b). Around the mean breaking point (Fig. 6b), the energy spectra of the difference $\zeta_{FRF} - \zeta_{SIO}$ appears as a white spectra whose energy level is 3 orders of magnitude lower than the swell energy peak (equivalent to a $\sim$ 1 millimeter error for a 1 m-amplitude wave). Similar behaviour is observed in the inner surf zone, where both dune and UAS FRF lidars accurately describe the $f^{-2}$ energy spectrum tail, which characterizes saw-tooth waves in this region (*e.g.*, Kirby and Kaihatu, 1997; Bonneton, 2023). The spectral analysis is complemented by cross-spectral analysis between the two corresponding timeseries, which provides a coherence between the two signals (Fig. 6cd) and the relative phase difference (Fig. 6ef). At both locations, the individually-gridded

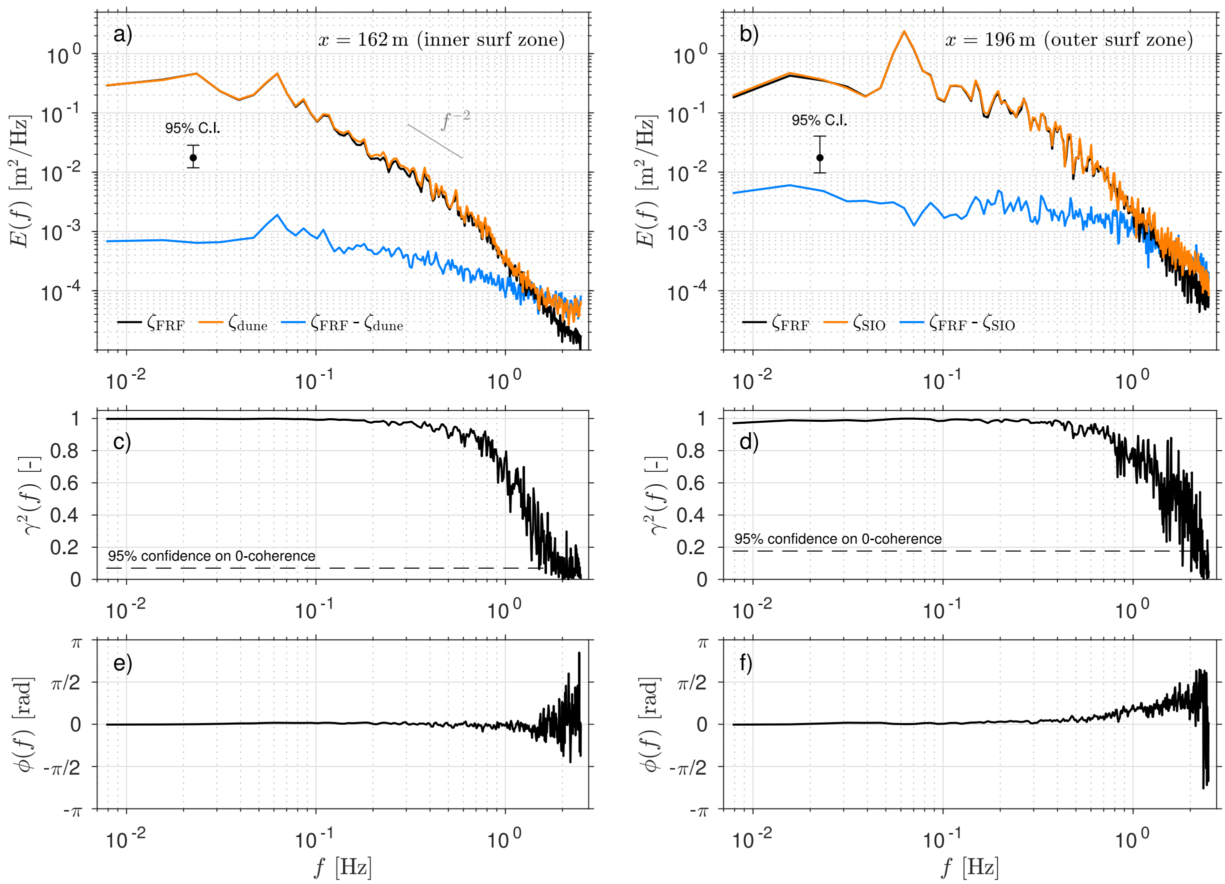


**Fig. 6.** Spectral and cross-spectral analysis of gridded free surface elevation $\zeta$ timeseries collected on 12 September (19:00–19:30 UTC, flight #1) by the three individual lidar systems (dune, FRF and SIO). Left panels focus on $\zeta$ timeseries collected in the inner surf zone ($x$ = 162 m, see Fig. fig:4a) by the dune and FRF UAS lidars while right panels concern $\zeta$ timeseries collected in the outer surf zone ($x$ = 195 m) by the FRF and SIO UAS lidars. Top panels (ab) show the spectral energy densities from the two lidar-derived timeseries at the respective locations and their difference. Middle (cd) and lower (ef) panels show the squared coherence between the corresponding two timeseries and their relative phase difference, respectively.

signals show a great coherence ($\gamma^2 > 0.99$, see Fig. 6cd) at the frequencies of interest for the Boussinesq-based depth inversion method, that is roughly between 0.05 Hz and 0.25 Hz. At these frequencies, the relative phase difference is near zero, meaning both lidars strictly measure the same signal, providing great confidence in the merging and the gridding procedures explained in the previous sub-section. This is consistent with the very weak energy levels computed from the difference timeseries shown in Fig. 6ab, as phase differences between the two series would result in greater energy, with well-defined peaks in spectra.

In this Section, we have developed a robust data processing chain for individual and/or multiple lidar data sources, which can originate from either single- or multibeam types of scanners. This allows for a great control over the characteristics and quality of the final gridded free surface elevation data, whose mean vertical accuracy is typically within the GPS accuracy, which is more than acceptable for most depth inversion applications. The next Section presents the depth inversion methodology itself, its specific implementation on lidar data as well as a novel approach for estimating an uncertainty on the final bathymetry estimate.

## 4. Implementation of the Boussinesq-based depth inversion approach to lidar datasets

### *4.1. Boussinesq-based depth inversion approach of Martins et al. (2023)*

Compared with other wave-based depth inversion algorithms based on optical imagery (*e.g.*, Holman et al., 2013; Simarro et al., 2019) or radar (*e.g.*, Honegger et al., 2019; Chernyshov et al., 2020), the methodology proposed by Martins et al. (2023) and applied here to lidar is novel in two main aspects: (1) it uses *direct* measurements of the free surface elevation, as opposed to other types of remote sensing technology that are affected by a modulation transfer function (*e.g.*, passive light or electromagnetic backscatter); and (2) it is based on a non-linear (Boussinesq) theory to predict frequency and amplitude dispersion effects on wavenumbers. Using geo-referenced lidar data has another significant advantage as it is not only the depth that can be estimated but a geo-referenced bathymetry thanks to the lidar-derived mean sea-surface elevation.

As with most existing algorithms, the depth inversion approach developed in Martins et al. (2023) for free surface elevation data estimates depth by matching, through a minimization procedure, observed and predicted wavenumbers at a given location. Wavenumbers are here predicted following the Boussinesq theory of Herbers et al. (2002), which estimates dominant wavenumber spectra $\kappa_{rms}$ directly from spectral and bispectral products of the free surface elevation $\zeta$ as:

$$\kappa_{rms}(\omega) = \frac{\omega}{\sqrt{gh}}\sqrt{1 + h\gamma_{fr}(\omega) - \frac{1}{h}\gamma_{am}(\omega)}, \tag{2}$$

with

$$\gamma_{fr}(\omega) = \frac{\omega^2}{3g} \tag{3}$$

$$\gamma_{am}(\omega) = \frac{3}{2E(\omega)}\int_{-\infty}^{\infty} \mathrm{Re}\left\{B(\omega', \omega-\omega')\right\} d\omega', \tag{4}$$

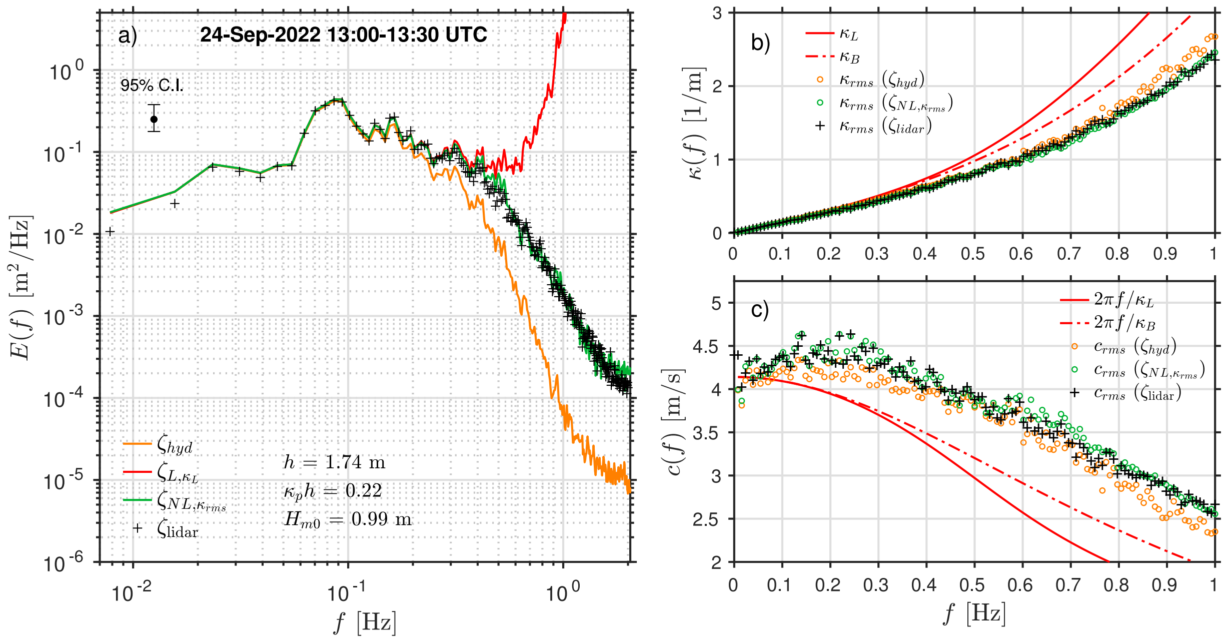


**Fig. 7.** Comparison of spectral and bispectral products computed on lidar and pressure-based free surface elevation timeseries collected at $x = 180$ m on the 24 of September (13:00–13:30 UTC, flight #20). Panel a) shows the spectral energy densities of the lidar ($\zeta_{\text{lidar}}$) direct measurements and the pressure-derived reconstructions: the hydrostatic $\zeta_{hyd}$, the fully-dispersive linear $\zeta_{L,\kappa_L}$ and the moderately dispersive non-linear $\zeta_{NL,\kappa_{rms}}$ of Martins et al. (2021a). Panel (b) compares the $\kappa_{rms}$ wavenumbers (Eq. (2)) computed from $\zeta_{hyd}$, $\zeta_{NL,\kappa_{rms}}$ and $\zeta_{\text{lidar}}$, together with linear and Boussinesq wavenumber predictions without amplitude dispersion effects ($\gamma_{am} = 0$ in Eq. (2)). Panel (c) shows the equivalent wave phase velocity spectra $c_{rms} = \omega/\kappa_{rms}$.

where $\omega = 2\pi f$ is the angular frequency, $h$ is the mean water depth, $E$ and $B$ are the spectral and bispectral densities of $\zeta$, respectively, and Re{.} denotes the real part. In Eq. (2), the leading-order term corresponds to the wavenumber for non-dispersive shallow-water waves. The terms $h\gamma_{fr}$ and $\gamma_{am}/h$ correspond to frequency and amplitude dispersion terms, respectively. Compared to the notation of Herbers et al. (2002), these dispersion terms were expressed in a way that $\gamma_{fr}$ and $\gamma_{am}$ are independent of $h$, which facilitates the depth inversion procedure.

Observed wavenumbers were obtained from cross-spectral analyses of free surface elevation data, following a similar strategy as in Martins et al. (2023). Obtaining robust estimates of wavenumber, or equivalently phase velocity spectra, in the field can be a challenging task (*e.g.*, Thornton and Guza, 1982; Elgar and Guza, 1985b), even more so when based on short ($\lesssim 30$ min) timeseries of potentially gappy lidar data. In order to estimate wavenumbers at a given location, we use all possible combinations of gauges around and equidistant to that location, and which were separated by a distance within 8–20% of the peak wavelength. The latter was computed from a first estimate of the bulk celerity and the peak wave period, estimated from spectral analysis at the most seaward lidar gauge. This procedure ensured that we obtain statistically robust estimates by averaging several individual estimates and removing statistically abnormal values. It also leverages potential wavelength-related bias that can be introduced when computing cross-spectra with a fixed distance between adjacent wave gauges. Details on the computation of spectral, bispectral and cross-spectral estimates and their statistical uncertainties are provided in Appendix. As lidars can be naturally gappy, special care needs to be taken for computing spectral products through Fourier analysis, which require continuous signals. Here, we only used data blocks with more than 90% returns, or equivalently with less than 10% of non-returns (NaNs). Blocks with more NaNs than this threshold were simply rejected. Gaps in surface elevation timeseries were then linearly interpolated prior to applying Fast Fourier Transforms (FFT). Given the cross-shore variation in the total amount of lidar data available for analysis (*e.g.*, see Fig. 4b for the example of flight #1), this resulted in a cross-shore variation of the number of data blocks used and the uncertainties of the spectral estimates.

The accuracy of spectral and bispectral estimates computed from gridded lidar data is here evaluated with comparisons against bottom pressure-based data from the RBR#5 ($x = 180$ m) collected during the flight #20 on the 24 of September (13:00–13:30 UTC). This corresponds to an outer surf zone situation, where the largest waves were starting to break at this location. Fig. 7a first shows the spectral energy densities of the free surface elevation directly measured by the UAS FRF lidar and that reconstructed from the bottom pressure signal. Three reconstructions are considered: the hydrostatic, the fully-dispersive linear (*e.g.*, Bishop and Donelan, 1987) and the moderately dispersive non-linear reconstruction of Martins et al. (2021a), in which a cutoff frequency at 0.7 Hz has been applied. The latter reconstruction method employs the $\kappa_{rms}$ Boussinesq predictions from Herbers et al. (2000) to predict non-linear effects in the wave dispersion relation (Eq. (2)). The moderately dispersive non-linear approach of Martins et al. (2021a) reconstructs the free surface elevation very accurately, with a correct description of energy levels up to very high frequencies (here shown up to 2 Hz, see Fig. 7a). Although the two sensors (lidar and pressure sensor) measured two distinct signals, an excellent match is obtained between $\kappa_{rms}$ spectra computed from the lidar and the $\zeta_{NL,\kappa_{rms}}$ reconstruction, showing that representative wavenumbers can be reliably estimated from short-duration lidar timeseries. As in Martins et al. (2021a), computing $\kappa_{rms}$ wavenumbers from the hydrostatic reconstruction (Herbers et al., 2002) provides a good first-order estimate of both frequency and amplitude dispersion effects, but with a $5-10\%$ overestimation that is well identified in wave phase velocity spectra in Fig. 7c. It is important to note that the reliability of $\kappa_{rms}$ spectra estimated from short lidar timeseries is also explained by the definition of $\kappa_{rms}$ itself (Eq. (2)). Indeed, though bispectral estimates naturally show large statistical uncertainties when computed over such short timeseries, the $\gamma_{am}$ term in Eq. (3) is actually computed from an integral over all frequencies of these bispectral estimates. This has for effect to significantly reduce the final uncertainty on $\kappa_{rms}(\omega)$ due to bispectrum computations.

### 4.2. Uncertainties on inverted water depths

The uncertainty on inverted water depths and hence, on the referenced bathymetry, directly depends on the type and number of observations used during the minimization procedure. Some differences are thus expected between the linear and Boussinesq approaches, since they used different spectral wave estimates. The objective of this Section is to implement a procedure to estimate an uncertainty on the inverted depths, such as the 95% confidence interval.

In practice, the mean water depth estimated at each observation location from Boussinesq theory corresponds to the depth $h$ that minimizes the following expression:

$$\sum_{\omega_i=\omega_{\min}}^{\omega_{\max}} \alpha_i \left( \kappa_{obs}(\omega_i) - \kappa_{rms}(\omega_i) \right)^2$$
$$= \sum_{\omega_i=\omega_{\min}}^{\omega_{\max}} \alpha_i \left( \kappa_{obs}(\omega_i) - \frac{\omega_i}{\sqrt{gh}} \sqrt{1 + h\gamma_{fr,1}(\omega_i) - \frac{1}{h}\gamma_{am}(\omega_i)} \right)^2, \tag{5}$$

where $\alpha_i$ are weights taken from the observed cross-spectra coherence and $[\omega_{\min}; \omega_{\max}]$ defines the frequency range over which the minimization is performed (Martins et al., 2023). The range of frequencies corresponds to $0.8 f_p$, $f_p$ being the peak frequency, to 0.25 Hz, an upper limit suggested by Herbers et al. (2002) for the validity of their theory under a wide range of conditions in shallow water depths as those considered here. As opposed to an algorithm like *cBathy*, where only few specific frequencies are picked (*e.g.*, the four most coherent ones), all frequencies within this range are here used for the inversion. Thus, the total number of spectral estimates depends on the frequency resolution, which is controlled by the length of the data block used for computing FFTs. In Eq. (5), statistical uncertainties lie within the observed wavenumber spectra $\kappa_{obs}$ (cross-spectrum), and in the predicted wavenumber spectra $\kappa_{rms}$ through the amplitude dispersion term $\gamma_{am}$ (spectra and integrated bispectra). As described in the Appendix, the statistical uncertainty for each spectral, bispectral and cross-spectral estimate can be theoretically calculated. However, how these translate into a depth uncertainty when such quantities are integrated (as for the bispectrum $B$, see Eq. (4)) or combined, is not. One possible manner to tackle this problem is through a Monte-Carlo simulation approach, which was implemented as follows. Knowing the uncertainties on individual spectral estimate, we randomly draw surrogate values for each estimate in its own 95% confidence interval, and compute a bathymetry using those surrogate values as observations. Here, the 95% confidence interval for each spectral estimate is approximated as $\pm 2\sigma$, $\sigma$ being the square-root of the theoretical spectral estimate variance (*i.e.*, the standard deviation; see also Appendix). By repeating this operation a certain number of realizations $N$ (here > 2000), this procedure provides a probability density function for the bathymetry, from which an uncertainty can be computed. A similar approach is also employed to evaluate the statistical uncertainty on the mean water depth computed from the linear wave dispersion relation, which minimizes the following expression:

$$\sum_{\omega_i=\omega_{\min}}^{\omega_{\max}} \alpha_i \left( h - \frac{1}{\kappa_{obs}(\omega_i)} \tanh^{-1} \left[ \frac{\omega_i^2}{\kappa_{obs}(\omega_i) g} \right] \right)^2 \tag{6}$$

It is worth noting that the uncertainty for the depth estimated using the linear wave dispersion originates only from the observed wavenumbers $\kappa_{obs}$, that is from the cross-spectral analyses.

An example of this Monte-Carlo approach is provided in Fig. 8 using data from the 12 of September (19:00–19:30 UTC, flight #1) in two distinct regions: an inner surf zone situation ($x = 175$ m, left panels) and a shoaling situation ($x = 225$ m, right panels). Wave phase velocity spectra ($c = \omega/\kappa(\omega)$) computed at these two locations from cross-spectral analyses of the free surface elevation data are shown in Fig. 8cd. The Monte-Carlo approach described above was applied to the corresponding wavenumber spectra $\kappa$, to get the inverted water depth probability density functions shown in Fig. 8ef. The first observation that can be made is that the probability density functions computed from Boussinesq and linear theory are of similar shape, the latter being slightly more peaky. Given that the linear theory estimates are only impacted by uncertainties originating from the observed cross-spectral values (see Eq. (6)), this indicates that statistical uncertainties on predicted wavenumbers $\kappa_{rms}$ (*i.e.*, spectral densities and bispectrum integrals, see Eq. (4)) are of minor importance. As already mentioned earlier, this is explained by the fact that bispectral products are integrated over all frequencies, significantly reducing the uncertainties associated with individual bispectral estimates. The estimated water depth distribution are almost symmetrical, displaying small but not null skewness values. For this reason, we use the median of the distribution as the final depth estimate throughout this manuscript. For all the cases analysed here, the 95% confidence interval was found to accurately match the $\pm 2\sigma_h$ range around the median value (maximum error < 1%), where $\sigma_h$ is the standard deviation of the distribution of depth estimates. Thus, in the following $\pm 2\sigma_h$ is used to compute the 95% confidence interval of the mean water depth estimate. This 95% confidence interval naturally increases with the water depth ($\sigma_h \sim 0.1$ m in the shoaling region against 0.04 m in the inner surf zone). However, once normalized by the surveyed local water depth, it remains relatively stable, representing approximately between 20 and 30% of the local depth, with a maximum reached around the mean breaking point. An important remark on the accuracy of the final depth estimate should be made at this point. For the selected flight, the Boussinesq theory provides excellent results in the shoaling region (relative error less than 5%, Fig. 8f), which contrasts with the relatively large overestimation obtained in the surf zone (Fig. 8e). It is important to stress that the uncertainty as computed here should be purely interpreted from a statistical point of view. It informs on the sensitivity of the final depth estimate to the observations and their statistical robustness, as opposed to the uncertainty associated with the choice of the underlying depth-inversion theoretical framework. The results of the depth inversion procedure described at these two specific locations are further described in the next section, dedicated to the bathymetric inversion results.

## 5. Nearshore topo-bathymetry reconstruction from lidars

In this Section, we analyse and discuss the performances of the methodology described above to reconstruct the topo-bathymetry cross-shore profiles along the transect $y \sim 945$ m. We focus on two flights, flights #1 (12 September 2022, 19:00–19:30 UTC) and #8 (13 September 2022, 19:00–19:30 UTC), for which the tide and wave conditions allowed a nearly-continuous coverage from the shoreline until the shoaling region, around $x \sim 250$ m.

During flight #1, the results previously presented in the shoaling ($x = 225$ m, Fig. 8a-c-e) and breaking ($x = 175$ m, Fig. 8b-d-f) wave regions are quite representative of the behaviour observed elsewhere within these specific regions (Fig. 9). In the shoaling region, Boussinesq phase velocity spectra $c_{rms}$ computed with the surveyed water depth accurately match the observed spectra $c_{obs}$ up to relatively high frequency ($f \sim 0.4$ Hz, see Fig. 8d). These good prediction skills are also found over the entire shoaling and outer surf region (up to $x = 210$ m), as shown with the good match between observed and Boussinesq predictions of the frequency-averaged phase velocities $\langle c \rangle_f$ (Fig. 9c). Overall, this suggests that the Boussinesq approximation of Herbers et al. (2002) is very accurate in predicting wave dispersive properties in shoaling and nearly breaking conditions, which is consistent with previous assessments in both field (Herbers et al., 2002) and laboratory (Martins et al., 2021a) conditions. Over this cross-section ($x = 210$–$250$ m), mean water depths are precisely estimated with the Boussinesq approach, leading to relative errors on the final and referenced bathymetry within $5 - 10\%$ (Fig. 9c), which corresponds to the accuracy obtained in laboratory conditions with similar methodology (Martins et al., 2023). These performances obtained for shoaling waves slightly deteriorate at the same location on the next day (flight #8, see Fig. 9d) but still remain satisfactory, with underestimations of the seabed elevation corresponding to $10 - 15\%$ of the local water depth.

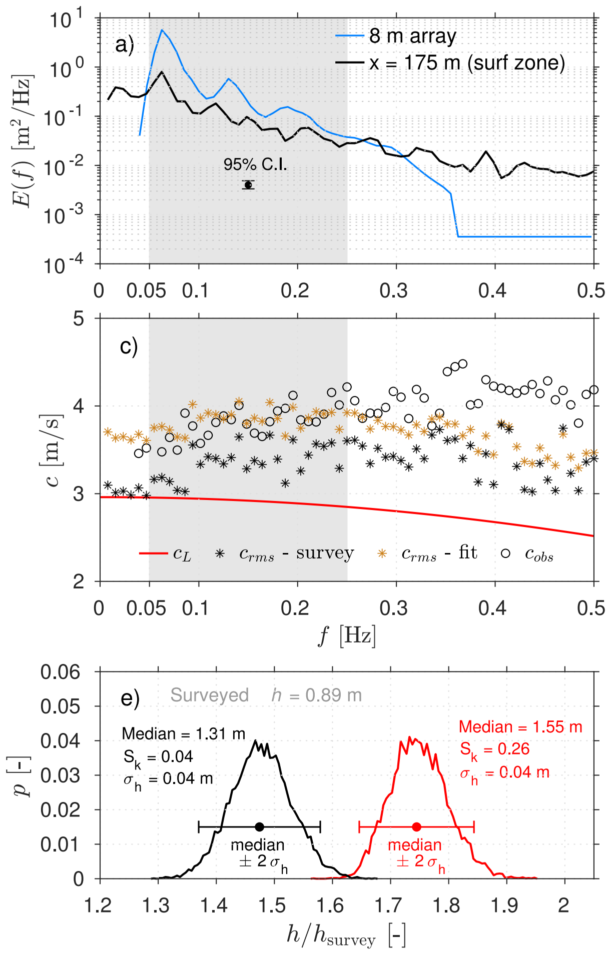


**Fig. 8.** Results from the Monte-Carlo approach to estimate the water depth in a surf zone (left panels) and shoaling (right panels) situation on the 12 of September (flight#1, 19:00–19:30 UTC). The top panels (ab) show the spectral energy densities of the lidar measurements at the corresponding location together with the bottom pressure-derived estimated at the 8 m array (offshore forcing). Central panels (cd) show a comparison between observed wave phase velocity spectra $c_{obs}$ with predictions by the Boussinesq theory ($c_{rms}$) and the linear wave dispersion $c_L$. Boussinesq predictions were made with two different water depths, the surveyed one and the depth that minimizes Eq. (5). Lower panels (ef) show the probability density function of the water depth estimates obtained with the Monte-Carlo simulation approach (Boussinesq: black; linear wave theory: red).

Within the surf zone, the performance of the Boussinesq-based depth inversion method deteriorates for flight #1, as evidenced by the negative bias on the predicted seabed elevation developing from $x \sim 195\,\text{m}$, and extending landwards until the shoreline (Fig. 9c). In terms of statistical errors, this translates into a net increase of the root-mean-square error (RMSE) passing from 8 cm outside the surf zone ($x \gtrsim 210\,\text{m}$) to 36 cm within the surf zone ($130 \lesssim x \lesssim 210\,\text{m}$), while the overall RMSE is 24 cm (including the beach topography). The drop in performances arising landwards of $x \sim 195\,\text{m}$ originates from the underestimation of phase velocities by the Boussinesq theory from this cross-shore position (Fig. 9a). Phase velocities $\langle c_{obs} \rangle_f$ observed in the surf zone are on average 0.5 m/s larger than those predicted by the Boussinesq theory with the surveyed water depth, while this is over 1 m/s for those predicted with the linear wave theory. This drop in performances observed during flight #1 contrasts with the excellent results obtained within the surf zone and up to the shoreline during flight #8 (Fig. 9d), with RMSE of 8 cm for $x \lesssim 200\,\text{m}$ (17 cm overall). Notably, the transition around the mean breaking point, between the shoaling and breaking wave region, is smooth during flight #8 both in terms of phase velocities and final seabed elevation.

In the present methodology, the impact of wave currents on cross-shore wave propagation speeds, and thus $\kappa(\omega)$, is ignored, which could explain the water depth overestimation obtained in the surf zone during flight #1. Wave group-forced surf zone eddies – ubiquitous at Duck, NC (Noyes et al., 2004; Long and Özkan-Haller, 2009; O'Dea et al., 2021b) – have the potential to generate transient mean cross-shore current reaching several dozens of cm/s. Alternatively, energetic swell breaking over 3D morphological features such as narrow channels have the potential to drive strong mean cross-shore currents (*e.g.*, see Dooley et al., 2024). The energetic swell experienced during flight #1 was characterized by a slight Northern offshore incidence of 5–10°(see Fig. 2). Combined with the 3D bottom feature developing on the Southern side of the monitored transect (see small rip channel around $y \sim 920\,\text{m}$, Fig. 1), this potentially caused relatively intense surf zone vortical motions, which could reach 0.4–0.5 m/s in the cross-shore direction. Conditions during flight #8 were much less energetic and non-linear, with smaller and shorter waves breaking over deeper water depths. This can be expressed in terms of non-linear parameter $\epsilon = H_{m0}/2h$, which reaches 0.5 in the inner surf zone during flight #1, compared to a value of 0.32 the following day ($x = 160\,\text{m}$ taken as reference). In terms of Ursell number, computed as the ratio between $\epsilon$ and the shallowness parameter $\mu = (\kappa_L(f_p)h)^2$, it is three times higher during flight #1 (50 against 16.5). The milder conditions encountered on the 13 of September are potentially less prone to generate surf zone eddies sufficiently strong to affect the waves' dispersive properties. To first order, an estimate of the mean current speed in the cross-shore direction could help improve the water depth estimate by accounting for it in the minimization procedure.

Interestingly, the contrasting conditions experienced during the two flights in terms of non-linearity also explain the contrasting performances obtained with the linear dispersion relation. For flight #8, the RMSE obtained with the linear approach is 0.45 cm overall (negative

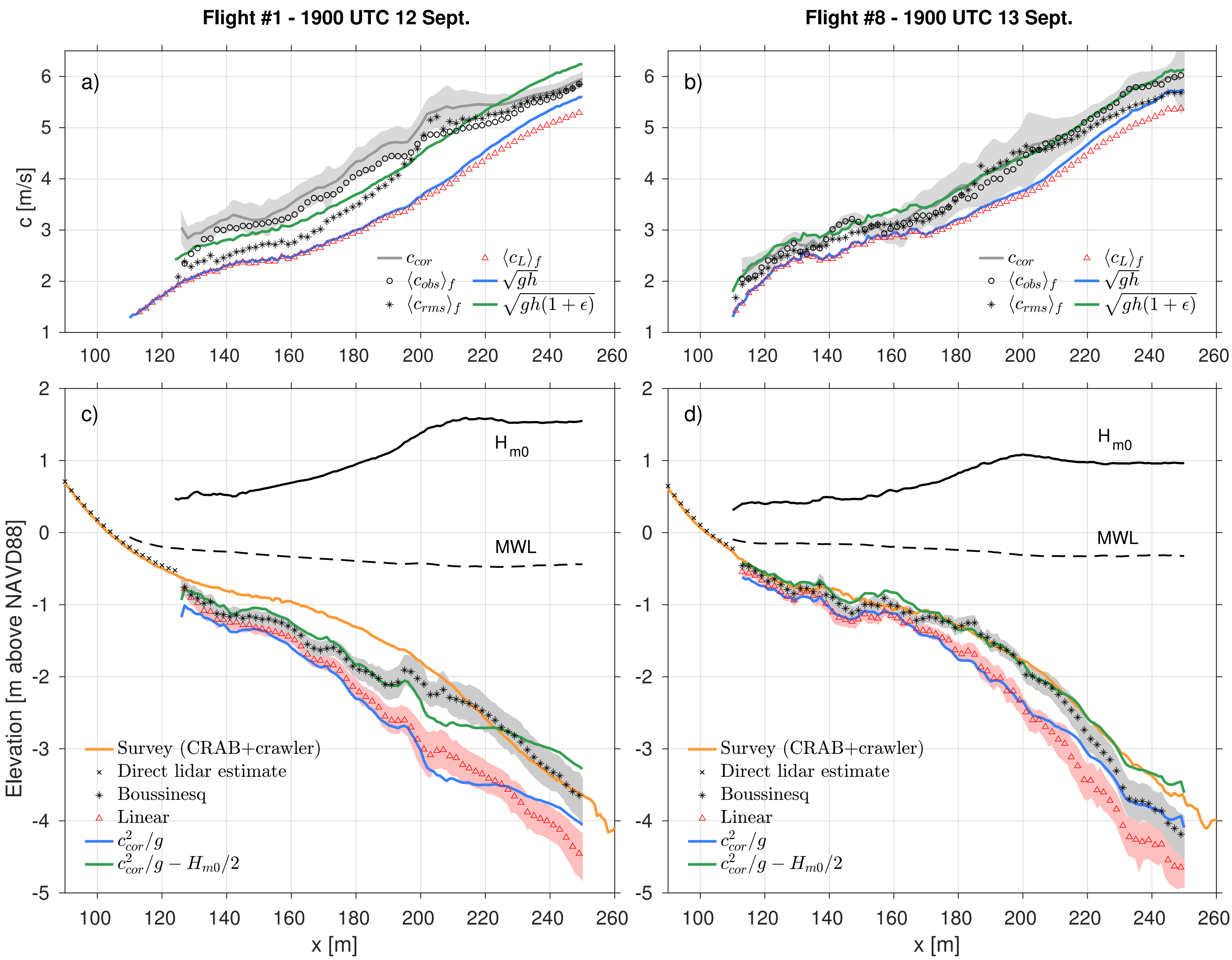


**Fig. 9.** Topo-bathymetry reconstruction for flight #1 (12 of September, 19:00–19:30 UTC; left panels) and flight #8 (13 of September, 19:00–19:30 UTC; right panels). The top panels (ab) show the cross-shore evolution of observed wave phase velocity spectra $\langle c_{obs}\rangle_f$, frequency-averaged over $[0.8f_p$, 0.25 Hz], with predictions by the Boussinesq theory $\langle c_{rms}\rangle_f$ and the linear wave dispersion $\langle c_L\rangle_f$. Bulk celerities $c_{cor}$ were estimated from simple surface elevation timeseries cross-correlations. Bottom panels (cd) show the topo-bathymetry reconstructed with each method. The error bar on the linear and Boussinesq prediction represent the 95% confidence interval obtained through the Monte Carlo method described in Section 4.2. For consistency, the bathymetry estimated with shallow water wave celerity predictors ($\sqrt{gh}$ and $\sqrt{gh(1+\epsilon)}$, with $\epsilon$ a non-linear parameter defined as $\epsilon = H_{m0}/2h$) are computed from the bulk celerity $c_{cor}$, not $\langle c_{obs}\rangle_f$. The direct lidar estimates of the beach face topography was extracted using a single lidar scan at the time the most seaward rundown limit was reached during the corresponding flight.

bias of 27 cm) while it reaches 0.56 cm overall during flight #1 (negative bias of 38 cm). This can be attributed to the stronger non-linear amplitude dispersive effects experienced during flight #1, as evidenced by the deviations of observed and predicted frequency-averaged phase velocities $\langle c\rangle_f$ from the shallow water wave celerity predictor $\sqrt{gh}$, computed with the surveyed mean wave depth (see Fig. 9a, and also Fig. 8d for phase velocity spectrum at $x = 225$ m). The differences are relatively small at the most seaward location surveyed here, between 0.2 and 0.3 m/s at $x = 250$ m depending on the flight. However, they exceed 1.2 m/s around the mean breaking point during flight #1 while these are at most 0.8 m/s during flight #8. This directly explains the limitations of the methods based on the linear wave dispersion relation or the shallow water wave predictor ($c \sim \sqrt{gh}$) to retrieve the water depth across the shoaling region, and the contrasting performances around the mean breaking point. Under the highly non-linear conditions of flight #1, the linear and shallow water-based approaches result in a final underestimation of the seabed elevation of the order of the water depth (100% error) around the mean breaking point ($x = 200-210$ m). Under the milder conditions of flight #8, these underestimations are of the order of 40% of the local water depth, which is closer to the numbers obtained by Martins et al. (2023) in similar shoaling, nearly-breaking situations. In these contrasting wave conditions, the results are significantly improved with the modified shallow water wave celerity predictor ($c \sim \sqrt{gh(1+\epsilon)}$), which treats non-linear amplitude effects empirically (Booij, 1981; Tissier et al., 2011; Martins et al., 2018). In laboratory conditions, Martins et al. (2023) showed that this predictor resulted in poor estimates of the mean depth in the shoaling and outer surf regions, with normalized errors typically within $20-40\%$. Here, this is the case only during flight #1 (40% error around $x \sim 210$ m), but this predictor actually improves the results during flight #8 compared to the Boussinesq-based method (Fig. 9c–d). In the surf zone, the performances of the two methods are relatively close, which is consistent with the results of Martins et al. (2023).

## 6. Summary and concluding remarks

Mapping the nearshore bathymetry and tracking its evolution over time – a prerequisite for studying beach morphological responses to storms – continues to challenge the coastal science community. Depth inversion techniques, which utilize remotely-sensed surface wave properties, are promising solutions that have been widely explored over the last few decades, mostly through video imagery. However, none of the solutions developed so far are capable of retrieving the surf zone bathymetry with sufficient accuracy to consider analysing the morphological evolution of this dynamic region. This study contributes towards this goal, by implementing the Boussinesq-based methodology of Martins et al. (2023) to multi-source shoaling and breaking wave lidar data collected in the field. In laboratory conditions, and for unidirectional waves, this methodology significantly advanced our capacity to retrieve the nearshore bathymetry by reducing errors to within 10% of the local water depth, including in the breaking wave region. These promising results motivated the planning of the BELS experiments that were presented herein.

Overall, the implementation of the Boussinesq-based depth inversion method of Martins et al. (2023) on field lidar data is considered to be successful. For the two flights considered in the previous Section, RMSEs less than $\sim 0.3$ m were obtained on the vertically-referenced topo-bathymetry elevations over a beach cross-shore section covering both shoaling and breaking situations. Furthermore, these results were obtained under contrasting wave conditions in terms of dispersion and non-linear intensity. For the most non-linear conditions analysed here (flight #1, 12 September 2022), a sudden drop in performances is obtained in the surf zone, where Boussinesq predictions underestimate the observed phase velocities by as much as 0.5 m/s. Here, this underestimation was attributed to the potential presence of mean cross-shore currents associated with energetic swell breaking in very shallow water depths and in the vicinity of a narrow channel. Another potential explanation lies in the assumption of a weakly non-linear wave field in the Boussinesq theory of Herbers and Burton (1997), which is used by Herbers et al. (2002) to derive their $\kappa_{rms}$ approximation. The degree of non-linearity found in the surf zone during flight #1 might be too strong to obtain depth estimates as accurate as during flight #8 or in laboratory conditions (Martins et al., 2023). Only through future field investigations covering more energetic conditions and with access to mean current fields, a more comprehensive understanding of the practical limitations of the present Boussinesq-based depth inversion method will be gained.

As described in Sections 3 and 4, the preparation phase of the field lidar data prior to proceeding with the Boussinesq-based depth inversion of Martins et al. (2023) required significant effort. These efforts were beneficial for improving and enhancing the robustness of (bi)spectral analysis of lidar data. Though working with gappy data slightly complicates data curation and analysis, the active remote sensing nature of lidar systems is a key advantage for inverting topo-bathymetric profiles compared to traditional passive remote sensing instrumentation. Indeed, a single lidar system allows for the estimation of wavenumbers not affected by modulation transfer function effects, the measurements of mean water levels – including the wave setup and its cross-shore variation – as well as the upper beach face, and its temporal evolution at the scale of wave groups. Thus, lidars are arguably the most powerful and well-suited remote sensing technology to capture, with sufficient spatio-temporal resolution the complex hydro-sediment interactions occurring at the land/sea interface, including during storms. Through the present methodology, or its future developments, future investigations under energetic conditions have the potential to reveal new insights into beach morphodynamics at temporal scales ranging from wave groups to entire storm events. However, barring any major technological breakthrough, the typical lidar coverage currently limits the present methodology to a few hundreds of meters in the cross-shore along a single cross-shore transect ($\sim$ 10–20 m-width). Though much valuable knowledge can already be gained with such coverage, exploring alternative approaches – such as remote sensing fusion techniques – could be the focus of concurrent efforts to improve spatial coverage and overcome the limitations of individual remote sensing technologies.

## Research data

Part of the data used in this research (bathymetry, water levels, and wave forcing) is publicly available through the U.S. Army Engineer Research and Development Centre at http://chlthredds.erdc.dren.mil/ The MATLAB toolboxes developed for this research are hosted at: https://github.com/ke-martins/lidar-toolbox/ In the 'examples' directory, a complete workflow example is included for reproducing the depth-inversion results at specific locations. The raw or pre-processed datasets can be made available upon reasonable request to the corresponding author.

## CRediT authorship contribution statement

**Kévin Martins:** Writing – original draft, Software, Methodology, Investigation, Funding acquisition, Formal analysis, Data curation, Conceptualization. **Katherine L. Brodie:** Writing – review & editing, Project administration, Investigation, Funding acquisition, Conceptualization. **Julia W. Fiedler:** Writing – review & editing, Software, Investigation, Data curation, Conceptualization. **Annika M. O'Dea:** Writing – review & editing, Investigation, Data curation. **Nicholas J. Spore:** Writing – review & editing, Investigation, Data curation. **Robert L. Grenzeback:** Investigation, Data curation. **Patrick J. Dickhudt:** Software, Investigation, Data curation. **Spicer Bak:** Investigation, Data curation. **Olivier de Viron:** Writing – review & editing, Software, Formal analysis. **Philippe Bonneton:** Writing – review & editing, Supervision.

## Declaration of competing interest

The authors declare that they have no known competing financial interests or personal relationships that could have appeared to influence the work reported in this paper.

## Acknowledgements

K.M. warmly thanks the entire FRF team for their welcome and particularly K.B. for making these experiments possible. The FRF participation was funded through the US Army Corps of Engineer's Coastal and Ocean Data Systems Program. J.W.F. and R.L.G.'s contribution to this work was funded by USACE grant W912HZ1920020. K.M. was funded through the European Union's Horizon 2020 research and innovation program under the Marie Skłodowska-Curie Grant Agreement 887867 (lidBathy). We thank the FRF operations team, in particular Nick Desimone and Chris Thoburn (AUGV operators), Jason Pipes (instrumentation mount fabrication and deployment strategy), and Shannon Brown and Ian W. Connery for their assistance during the UAS flights. We also thank Falk Feddersen for lending his multibeam lidar and UAS for these experiments.

## Appendix. Spectral, cross-spectral and bispectral estimates of $\zeta$

The present depth inversion procedure requires the computation of spectral, cross-spectral and bispectral estimates of the free surface elevation $\zeta$ collected by lidars. More details on these quantities, and their associated uncertainty, are given in this Appendix.

Let $E$ and $B$ denote the spectral and bispectral densities of the time-varying detrended free surface elevation signal $\zeta(t)$ at location $x$, respectively. The energy spectra $E$ of $\zeta$ is here given by:

$$E(\omega) = 2\,\mathcal{E}\left[A(\omega)\,A^{*}(\omega)\right], \tag{A.1}$$

where $\omega = 2\pi f$ is the angular frequency, $A$ are the complex Fourier coefficients of $\zeta$, $^*$ denotes the complex conjugate and $\mathcal{E}$ is an expected, or ensemble-average, value. This ensemble-average is estimated using Welch's overlapped segment averaging spectral estimator. Data blocks were tapered using a Hann window and an overlap of 75% was used as it maximizes the effective number of degrees of freedom. For non-fully independent overlapping segments of real-world physical data, estimating the effective number of degrees of freedom of a spectral estimate is non-trivial (*e.g.*, Elgar, 1987). Here, we used the approximation for the equivalent number of degrees of freedom for different window techniques and overlap given by Percival and Walden (1993, their Eq. 292b). As already mentioned in the manuscript, only data blocks of sufficient "quality" (typically more than 90% of returns) are used. Thus, the cross-shore variation in the total amount of lidar data used to compute spectral estimates naturally results in a cross-shore variation of the equivalent number of degrees of freedom and the associated uncertainties. The 95% confidence interval is classically computed from the chi-square distribution using this estimate of the equivalent number of degrees of freedom.

The bispectrum of $\zeta$ is here computed following Kim and Powers (1979) as:

$$B(\omega_1, \omega_2) = \mathcal{E}\left[A(\omega_1)\, A(\omega_2)\, A^*(\omega_1 + \omega_2)\right]. \tag{A.2}$$

These bispectral estimates are computed following a similar Welch approach as above except that data segments are not tapered. Indeed, as already observed in Martins et al. (2021b), tapering data blocks results in a mismatch between bispectrum-derived and statistical definitions of skewness and asymmetry. Here, it also resulted in larger predicted wave phase velocities compared values obtained without tapering data blocks, potentially because of an overestimated contribution from non-linear amplitude effects in the Boussinesq $\kappa_{rms}$ formulation (*i.e.*, of non-linear coupling). Thus, we here choose to preserve the third-order moments of the timeseries (*e.g.*, skewness and asymmetry) by not tapering the segments. Note that this is consistent with the bispectral estimates in recent studies by the first author for quantifying non-linear effects in nearshore wave dispersion relations, both for depth inversion purposes (Martins et al., 2021a) or for recovering the surface elevation from bottom hydrodynamic measurements (Martins et al., 2023). Finally, the variance of bispectral estimate is required in the Monte-Carlo approach developed above for computing a 95% confidence limit on the final mean water depth estimate. This variance is given by Kim and Powers (1979) as:

$$\mathrm{var}\left(B(\omega_1, \omega_2)\right) \approx \frac{1}{M} P(\omega_1)\, P(\omega_2)\, P(\omega_1 + \omega_2)\left[1 - b^2(\omega_1, \omega_2)\right], \tag{A.3}$$

where $M$ is the number of segments, $P$ is the power spectrum (related to the energy spectrum as $P = E/2$) and $b$ is a quadratic correlation coefficient, sometimes referred to as the bicoherence:

$$b^2(\omega_1, \omega_2) = \frac{|B(\omega_1, \omega_2)|^2}{\mathcal{E}\left[\,|A(\omega_1)\, A(\omega_2)|\,\right] \mathcal{E}\left[\,|A(\omega_1 + \omega_2)|^2\right]} \tag{A.4}$$

Observed (dominant) wavenumber spectra $\kappa_{obs}$ are estimated using cross-spectral analyses performed on lidar-derived $\zeta$ data following the methodology developed in Martins et al. (2021b) and Martins et al. (2023) for spatially-dense wave gauges. Let $C_{x_1,x_2}$ denote the cross-spectrum computed from the detrended free surface elevation signal $\zeta$ measured at two adjacent gauges located at cross-shore positions $x_1$ and $x_2$:

$$C_{x_1,x_2}(\omega) = \mathcal{E}\left[A_{x_1}(\omega)\, A^*_{x_2}(\omega)\right] \tag{A.5}$$

The (squared) coherence $\gamma^2(\omega)$ and relative phase $\phi(\omega)$ spectra computed between $x_1$ and $x_2$ are then given by:

$$\gamma^2_{x_1,x_2}(\omega) = \frac{|C_{x_1,x_2}(\omega)|^2}{C_{x_1,x_1}(\omega)\, C_{x_2,x_2}(\omega)} \tag{A.6}$$

$$\phi_{x_1,x_2}(\omega) = \arctan\left[\frac{\mathrm{Im}\{C_{x_1,x_2}(\omega)\}}{\mathrm{Re}\{C_{x_1,x_2}(\omega)\}}\right], \tag{A.7}$$

where $\mathrm{Re}\{\cdot\}$ and $\mathrm{Im}\{\cdot\}$ are the real and imaginary parts of the cross-spectra, respectively. The time delay (in sec) per frequency is obtained from the unwrapped phase $\phi^{unw}$. In the case of progressive nearshore waves in the sea-swell range of frequencies, phase jumps are clearly identified so that the delays per frequency can be estimated unambiguously. The wavenumber $\kappa_{obs}(\omega)$ magnitude is finally computed as:

$$\kappa_{obs}(\omega) = \phi^{unw}_{x_1,x_2}(\omega) \big/ \Delta x, \tag{A.8}$$

where $\Delta x$ is the spacing between the two wave gauges. The phase velocity spectra are also readily obtained as $c_{obs}(\omega) = \omega/\kappa_{obs}(\omega)$. $\kappa_{obs}$ refers to the single-valued cross-shore wavenumber magnitude and is representative of the energy spread across both forced and free components at a given frequency (Herbers et al., 2002; Martins et al., 2021b). In practice, $\kappa_{obs}$ and $c_{obs}$ are estimates at the location $x_m = (x_1 + x_2)/2$ of the dominant wavenumber (in an energy-averaged sense) and the corresponding cross-shore propagation velocity, respectively. As for spectra and bispectra, cross-spectral estimates are computed using Welch's method using blocks of data overlapping by 75% and tapered with a Hann window. Given the linear relation between wavenumbers and the cross-spectrum phase, the variance of the phase can be used to estimate the uncertainty of wavenumber estimates. The phase variance is here approximated following Hinich and Clay (1968) as:

$$\mathrm{var}\left(\phi_{x_1,x_2}(\omega)\right) \approx \frac{1}{2M}\left[\gamma^{-2}_{x_1,x_2}(\omega) - 1\right]. \tag{A.9}$$

Similar to the variance of bispectral estimate, this is used above for computing a 95% confidence limit on the final mean water depth estimate through a Monte-Carlo approach described in the main text.

## Data availability

Data statement made in the manuscript and in cover letter.

## References


Almar, R., Bonneton, P., Sénéchal, N., Roelvink, D., 2008. Wave celerity from video imaging: a new method. In: Proceedings of the 32nd Conference on Coastal Engineering, Hamburg, Germany. World Scientific Publishing Company, pp. 661–673. http://dx.doi.org/10.1142/9789814277426_0056.

Almeida, L.P., Masselink, G., Russell, P.E., Davidson, M.A., 2015. Observations of gravel beach dynamics during high energy wave conditions using a laser scanner. Geomorphology 228, 15–27. http://dx.doi.org/10.1016/j.geomorph.2014.08.019.

Apotsos, A., Raubenheimer, B., Elgar, S., Guza, R.T., Smith, J.A., 2007. Effects of wave rollers and bottom stress on wave setup. J. Geophys. Res.: Ocean. 112 (C2), http://dx.doi.org/10.1029/2006JC003549.

Bak, A.S., Durkin, P., Bruder, B., Saenz, M.J., Forte, M.F., Brodie, K.L., 2023. Amphibious uncrewed ground vehicle for coastal surfzone survey. J. Surv. Eng. 149 (4), 04023011. http://dx.doi.org/10.1061/JSUED2.SUENG-1381.

Bayle, P.M., Blenkinsopp, C.E., Martins, K., Kaminsky, G.M., Weiner, H.M., Cottrell, D., 2023. Swash-by-swash morphology change on a dynamic cobble berm revetment: High-resolution cross-shore measurements. Coast. Eng. 184, 104341. http://dx.doi.org/10.1016/j.coastaleng.2023.104341.

Bergsma, E.W.J., Almar, R., 2018. Video-based depth inversion techniques, a method comparison with synthetic cases. Coast. Eng. 138, 199–209. http://dx.doi.org/10.1016/j.coastaleng.2018.04.025.

Bergsma, E.W.J., Almar, R., de Almeida, L.P.M., Sall, M., 2019. On the operational use of UAVs for video-derived bathymetry. Coast. Eng. 152, 103527. http://dx.doi.org/10.1016/j.coastaleng.2019.103527.

Bergsma, E.W.J., Conley, D.C., Davidson, M.A., O'Hare, T.J., 2016. Video-based nearshore bathymetry estimation in macro-tidal environments. Mar. Geol. 374, 31–41. http://dx.doi.org/10.1016/j.margeo.2016.02.001.

Bishop, C.T., Donelan, M.A., 1987. Measuring waves with pressure transducers. Coast. Eng. 11 (4), 309–328. http://dx.doi.org/10.1016/0378-3839(87)90031-7.

Blenkinsopp, C.E., Hunter, A.J., Baldock, T.E., Bayle, P.M., Bosboom, J., Conley, D., Masselink, G., 2024. Repeatability of beach morphology change under identical wave forcing. Coast. Eng. 189, 104485. http://dx.doi.org/10.1016/j.coastaleng.2024.104485.

Blenkinsopp, C.E., Mole, M.A., Turner, I.L., Peirson, W.L., 2010. Measurements of the time-varying free-surface profile across the swash zone obtained using an industrial (LIDAR). Coast. Eng. 57 (11–12), 1059–1065. http://dx.doi.org/10.1016/j.coastaleng.2010.07.001.

Blenkinsopp, C.E., Turner, I.L., Allis, M.J., Peirson, W.L., Garden, L.E., 2012. Application of LiDAR technology for measurement of time-varying free-surface profiles in a laboratory wave flume. Coast. Eng. 68, 1–5. http://dx.doi.org/10.1016/j.coastaleng.2012.04.006.

Bonneton, P., 2023. Energy and dissipation spectra of waves propagating in the inner surf zone. J. Fluid Mech. 977, A48. http://dx.doi.org/10.1017/jfm.2023.878.

Booij, N., 1981. Gravity Waves on Water with Non-Uniform Depth and Current (Ph.D. thesis). Technische Hogeschool, Delft (Netherlands).

Bouvier, C., Balouin, Y., Castelle, B., Valentini, N., 2020. Video depth inversion at a microtidal site exposed to prevailing low-energy short-period waves and episodic severe storms. J. Coast. Res. 95, 1021–1026. http://dx.doi.org/10.2112/SI95-199.1.

Brodie, K.L., Palmsten, M.L., Hesser, T.J., Dickhudt, P.J., Raubenheimer, B., Ladner, H., Elgar, S., 2018. Evaluation of video-based linear depth inversion performance and applications using altimeters and hydrographic surveys in a wide range of environmental conditions. Coast. Eng. 136, 147–160. http://dx.doi.org/10.1016/j.coastaleng.2018.01.003.

Brodie, K.L., Raubenheimer, B., Elgar, S., Slocum, R.K., McNinch, J.E., 2015. Lidar and pressure measurements of inner-surfzone waves and setup. J. Atmos. Ocean. Technol. 32 (10), 1945–1959. http://dx.doi.org/10.1175/JTECH-D-14-00222.1.

Brodie, K.L., Slocum, R.K., McNinch, J.E., 2012. New insights into the physical drivers of wave runup from a continuously operating terrestrial laser scanner. In: Oceans, 2012. pp. 1–8. http://dx.doi.org/10.1109/OCEANS.2012.6404955.

Catalán, P.A., Haller, M.C., 2008. Remote sensing of breaking wave phase speeds with application to non-linear depth inversions. Coast. Eng. 55 (1), 93–111. http://dx.doi.org/10.1016/j.coastaleng.2007.09.010.

Chernyshov, P., Vrecica, T., Streßer, M., Carrasco, R., Toledo, Y., 2020. Rapid wavelet-based bathymetry inversion method for nearshore X-band radars. Remote Sens. Environ. 240, 111688. http://dx.doi.org/10.1016/j.rse.2020.111688.

Collins, A.M., Brodie, K.L., Bak, A.S., Hesser, T.J., Farthing, M.W., Lee, J., Long, J.W., 2020. Bathymetric inversion and uncertainty estimation from synthetic surf-zone imagery with machine learning. Remote. Sens. 12 (20), http://dx.doi.org/10.3390/rs12203364.

Dooley, C., Elgar, S., Raubenheimer, B., 2024. Field observations of surfzone vorticity. Geophys. Res. Lett. 51 (20), http://dx.doi.org/10.1029/2024GL111402, e2024GL111402.

Dugan, J.P., Piotrowski, C.C., Williams, J.Z., 2001. Water depth and surface current retrievals from airborne optical measurements of surface gravity wave dispersion. J. Geophys. Res.: Ocean. 106 (C8), 16903–16915. http://dx.doi.org/10.1029/2000JC000369.

Elgar, S., 1987. Bias of effective degrees of freedom of a spectrum. J. Waterw. Port, Coast. Ocean. Eng. 113 (1), 77–82. http://dx.doi.org/10.1061/(ASCE)0733-950X(1987)113:1(77).

Elgar, S., Guza, R.T., 1985a. Observations of bispectra of shoaling surface gravity waves. J. Fluid Mech. 161, 425–448. http://dx.doi.org/10.1017/S0022112085003007.

Elgar, S., Guza, R.T., 1985b. Shoaling gravity waves: comparisons between field observations, linear theory, and a nonlinear model. J. Fluid Mech. 158, 47–70. http://dx.doi.org/10.1017/S0022112085002543.

Feddersen, F., Marques, O.B., MacMahan, J.H., Grenzeback, R.L., 2024. Estimating directional wave spectra properties in nonbreaking waves from a UAS-mounted multibeam lidar. J. Atmos. Ocean. Technol. 41 (5), 515–530. http://dx.doi.org/10.1175/JTECH-D-23-0129.1.

Fiedler, J.W., Brodie, K.L., McNinch, J.E., Guza, R.T., 2015. Observations of runup and energy flux on a low-slope beach with high-energy, long-period ocean swell. Geophys. Res. Lett. 42 (22), 9933–9941. http://dx.doi.org/10.1002/2015GL066124.

Fiedler, J.W., Kim, L., Grenzeback, R.L., Young, A.P., Merrifield, M.A., 2021. Enhanced surf zone and wave runup observations with hovering drone-mounted lidar. J. Atmos. Ocean. Technol. 38 (11), 1967–1978. http://dx.doi.org/10.1175/JTECH-D-21-0027.1.

Gawehn, M., de Vries, S., Aarninkhof, S., 2021. A self-adaptive method for mapping coastal bathymetry on-the-fly from wave field video. Remote. Sens. 13 (23), http://dx.doi.org/10.3390/rs13234742.

Gawehn, M., van Dongeren, A., de Vries, S., Swinkels, C., Hoekstra, R., Aarninkhof, S., Friedman, J., 2020. The application of a radar-based depth inversion method to monitor near-shore nourishments on an open sandy coast and an ebb-tidal delta. Coast. Eng. 159, 103716. http://dx.doi.org/10.1016/j.coastaleng.2020.103716.

Grilli, S.T., 1998. Depth inversion in shallow water based on nonlinear properties of shoaling periodic waves. Coast. Eng. 35 (3), 185–209. http://dx.doi.org/10.1016/S0378-3839(98)00035-0.

Guérin, T., Bertin, X., Coulombier, T., de Bakker, A., 2018. Impacts of wave-induced circulation in the surf zone on wave setup. Ocean. Model. 123, 86–97. http://dx.doi.org/10.1016/j.ocemod.2018.01.006.

Herbers, T.H.C., Burton, M.C., 1997. Nonlinear shoaling of directionally spread waves on a beach. J. Geophys. Res.: Ocean. 102 (C9), 21101–21114. http://dx.doi.org/10.1029/97JC01581.

Herbers, T.H.C., Elgar, S., Sarap, N.A., Guza, R.T., 2002. Nonlinear dispersion of surface gravity waves in shallow water. J. Phys. Oceanogr. 32 (4), 1181–1193. http://dx.doi.org/10.1175/1520-0485(2002)032<1181:NDOSGW>2.0.CO;2.

Herbers, T.H.C., Russnogle, N.R., Elgar, S., 2000. Spectral energy balance of breaking waves within the surf zone. J. Phys. Oceanogr. 30 (11), 2723–2737.

Hinich, M.J., Clay, C.S., 1968. The application of the discrete Fourier transform in the estimation of power spectra, coherence, and bispectra of geophysical data. Rev. Geophys. 6 (3), 347–363. http://dx.doi.org/10.1029/RG006i003p00347.

Holland, T.K., 2001. Application of the linear dispersion relation with respect to depth inversion and remotely sensed imagery. IEEE Trans. Geosci. Remote Sens. 39 (9), 2060–2072. http://dx.doi.org/10.1109/36.951097.

Holman, R., Haller, M.C., 2013. Remote sensing of the nearshore. Annu. Rev. Mar. Sci. 5 (1), 95–113. http://dx.doi.org/10.1146/annurev-marine-121211-172408, PMID: 22809186.

Holman, R., Plant, N., Holland, T., 2013. cBathy: A robust algorithm for estimating nearshore bathymetry. J. Geophys. Res.: Ocean. 118 (5), 2595–2609. http://dx.doi.org/10.1002/jgrc.20199.

Honegger, D.A., Haller, M.C., Holman, R.A., 2019. High-resolution bathymetry estimates via X-band marine radar: 1. beaches. Coast. Eng. 149, 39–48. http://dx.doi.org/10.1016/j.coastaleng.2019.03.003.

Irish, J.L., Lillycrop, W.J., 1999. Scanning laser mapping of the coastal zone: the SHOALS system. ISPRS J. Photogramm. Remote Sens. 54 (2–3), 123–129.

Irish, J.L., Wozencraft, J.M., Cunningham, A.G., Giroud, C., 2006. Nonintrusive measurement of ocean waves: Lidar wave gauge. J. Atmos. Ocean. Technol. 23, 1559–1572. http://dx.doi.org/10.1175/JTECH1936.1.

Kim, L.N., Brodie, K.L., Cohn, N.T., Giddings, S.N., Merrifield, M., 2023a. Observations of beach change and runup, and the performance of empirical runup parameterizations during large storm events. Coast. Eng. 184, 104357. http://dx.doi.org/10.1016/j.coastaleng.2023.104357.

Kim, B., Noh, H., Park, Y.S., Lee, M., 2023b. Non-spectral linear depth inversion using drone-acquired wave field imagery. Appl. Ocean Res. 138, 103625. http://dx.doi.org/10.1016/j.apor.2023.103625.

Kim, Y.C., Powers, E.J., 1979. Digital bispectral analysis and its applications to nonlinear wave interactions. IEEE Trans. Plasma Sci. 7 (2), 120–131. http://dx.doi.org/10.1109/TPS.1979.4317207.

Kirby, J.T., Kaihatu, J.M., 1997. Structure of frequency domain models for random wave breaking. In: Proceedings of the 25th Conference on Coastal Engineering, Orlando, Florida. pp. 1144–1155. http://dx.doi.org/10.1061/9780784402429.089.

Lange, A.M.Z., Fiedler, J.W., Merrifield, M.A., Guza, R.T., 2023. UAV video-based estimates of nearshore bathymetry. Coast. Eng. 185, 104375. http://dx.doi.org/10.1016/j.coastaleng.2023.104375.

Lippmann, T.C., Holman, R.A., 1991. Phase speed and angle of breaking waves measured with video techniques. In: Proceedings of Coastal Sediments '91, American Society of Civil Engineers, New York. pp. 542–556.

Long, C.E., 1996. Index and bulk parameters for frequency-direction spectra measured at CERC Field Research Facility, June 1994 to August 1995. Miscellaneous Paper CERC-96-6, US Army Corps of Engineers Waterways Experiment Station.

Long, J.W., Özkan-Haller, H.T., 2009. Low-frequency characteristics of wave group–forced vortices. J. Geophys. Res.: Ocean. 114 (C8), http://dx.doi.org/10.1029/2008JC004894.

Lyzenga, D.R., 1985. Shallow-water bathymetry using combined lidar and passive multispectral scanner data. Int. J. Remote Sens. 6 (1), 115–125.

Martins, K., Bertin, X., Mengual, B., Pezerat, M., Lavaud, L., Guérin, T., Zhang, Y.J., 2022. Wave-induced mean currents and setup over barred and steep sandy beaches. Ocean. Model. 179, 102110. http://dx.doi.org/10.1016/j.ocemod.2022.102110.

Martins, K., Blenkinsopp, C.E., Almar, R., Zang, J., 2017a. The influence of swash-based reflection on surf zone hydrodynamics: a wave-by-wave approach. Coast. Eng. 122, 27–43. http://dx.doi.org/10.1016/j.coastaleng.2017.01.006.

Martins, K., Blenkinsopp, C.E., Deigaard, R., Power, H.E., 2018. Energy dissipation in the inner surf zone: New insights from LiDAR-based roller geometry measurements. J. Geophys. Res.: Ocean. 123 (5), 3386–3407. http://dx.doi.org/10.1029/2017JC013369.

Martins, K., Blenkinsopp, C.E., Power, H.E., Bruder, B., Puleo, J.A., Bergsma, E.W.J., 2017b. High-resolution monitoring of wave transformation in the surf zone using a LiDAR scanner array. Coast. Eng. 128, 37–43. http://dx.doi.org/10.1016/j.coastaleng.2017.07.007.

Martins, K., Blenkinsopp, C.E., Zang, J., 2016. Monitoring individual wave characteristics in the inner surf with a 2-dimensional laser scanner (LiDAR). J. Sensors 2016, 1–11. http://dx.doi.org/10.1155/2016/7965431.

Martins, K., Bonneton, P., de Viron, O., Turner, I.L., Harley, M.D., Splinter, K., 2023. New perspectives for nonlinear depth-inversion of the nearshore using Boussinesq theory. Geophys. Res. Lett. 50 (2), http://dx.doi.org/10.1029/2022GL100498, e2022GL100498.

Martins, K., Bonneton, P., Lannes, D., Michallet, H., 2021a. Relation between orbital velocities, pressure, and surface elevation in nonlinear nearshore water waves. J. Phys. Oceanogr. 51 (11), 3539–3556. http://dx.doi.org/10.1175/JPO-D-21-0061.1.

Martins, K., Bonneton, P., Michallet, H., 2021b. Dispersive characteristics of non-linear waves propagating and breaking over a mildly sloping laboratory beach. Coast. Eng. 167, 103917. http://dx.doi.org/10.1016/j.coastaleng.2021.103917.

Matsuba, Y., Sato, S., 2018. Nearshore bathymetry estimation using UAV. Coast. Eng. J. 60 (1), 51–59. http://dx.doi.org/10.1080/21664250.2018.1436239.

Nicolae-Lerma, A., Pedreros, R., Robinet, A., Sénéchal, N., 2017. Simulating wave setup and runup during storm conditions on a complex barred beach. Coast. Eng. 123, 29–41. http://dx.doi.org/10.1016/j.coastaleng.2017.01.011.

Noyes, T.J., Guza, R.T., Elgar, S., Herbers, T.H.C., 2004. Field observations of shear waves in the surf zone. J. Geophys. Res.: Ocean. 109 (C1), http://dx.doi.org/10.1029/2002JC001761.

O'Dea, A., Brodie, K., 2024. Analysis of beach cusp formation and evolution using high-frequency 3D lidar scans. J. Geophys. Res.: Earth Surf. 129 (2), http://dx.doi.org/10.1029/2023JF007472, e2023JF007472.

O'Dea, A., Brodie, K., Elgar, S., 2021a. Field observations of the evolution of plunging-wave shapes. Geophys. Res. Lett. 48 (16), http://dx.doi.org/10.1029/2021GL093664, e2021GL093664.

O'Dea, A., Brodie, K.L., Hartzell, P., 2019. Continuous coastal monitoring with an automated terrestrial lidar scanner. J. Mar. Sci. Eng. 7 (2), http://dx.doi.org/10.3390/jmse7020037.

O'Dea, A., Kumar, N., Haller, M.C., 2021b. Simulations of the surf zone Eddy field and cross-shore exchange on a nonidealized bathymetry. J. Geophys. Res.: Ocean. 126 (5), http://dx.doi.org/10.1029/2020JC016619, e2020JC016619.

Percival, D.B., Walden, A.T., 1993. Spectral Analysis for Physical Applications. Cambridge University Press.

Phillips, M.S., Blenkinsopp, C.E., Splinter, K.D., Harley, M.D., Turner, I.L., 2019. Modes of berm and beachface recovery following storm reset: Observations using a continuously scanning lidar. J. Geophys. Res.: Earth Surf. 124 (3), 720–736. http://dx.doi.org/10.1029/2018JF004895.

Plant, N.G., Holland, K.T., Haller, M.C., 2008. Ocean wavenumber estimation from wave-resolving time series imagery. IEEE Trans. Geosci. Remote Sens. 46 (9), 2644–2658. http://dx.doi.org/10.1109/TGRS.2008.919821.

Reineman, B.D., Lenain, L., Castel, D., Melville, W.K., 2009. A portable airborne scanning lidar system for ocean and coastal applications. J. Atmos. Ocean. Technol. 26 (12), 2626–2641. http://dx.doi.org/10.1175/2009JTECHO703.1.

Rodríguez-Padilla, I., Castelle, B., Marieu, V., Morichon, D., 2022. Video-based nearshore bathymetric inversion on a geologically constrained mesotidal beach during storm events. Remote. Sens. 14 (16), http://dx.doi.org/10.3390/rs14163850.

Salameh, E., Frappart, F., Almar, R., Baptista, P., Heygster, G., Lubac, B., Raucoules, D., Almeida, L.P., Bergsma, E.W.J., Capo, S., De Michele, M., Idier, D., Li, Z., Marieu, V., Poupardin, A., Silva, P.A., Turki, I., Laignel, B., 2019. Monitoring beach topography and nearshore bathymetry using spaceborne remote sensing: A review. Remote. Sens. 11 (19), http://dx.doi.org/10.3390/rs11192212.

Santos, D., Abreu, T., Silva, P.A., Santos, F., Baptista, P., 2022. Nearshore bathymetry retrieval from wave-based inversion for video imagery. Remote. Sens. 14 (9), http://dx.doi.org/10.3390/rs14092155.

Sherwood, C.R., van Dongeren, A., Doyle, J., Hegermiller, C.A., Hsu, T.J., Kalra, T.S., Olabarrieta, M., Penko, A.M., Rafati, Y., Roelvink, D., van der Lugt, M., Veeramony, J., Warner, J.C., 2022. Modeling the morphodynamics of coastal responses to extreme events: What shape are we in? Annu. Rev. Mar. Sci. 14 (1), 457–492. http://dx.doi.org/10.1146/annurev-marine-032221-090215, PMID: 34314599.

Simarro, G., Calvete, D., Luque, P., Orfila, A., Ribas, F., 2019. UBathy: A new approach for bathymetric inversion from video imagery. Remote. Sens. 11 (23), http://dx.doi.org/10.3390/rs11232722.

Stockdon, H.F., Holman, R.A., 2000. Estimation of wave phase speed and nearshore bathymetry from video imagery. J. Geophys. Res.: Ocean. 105 (C9), 22015–22033. http://dx.doi.org/10.1029/1999JC000124.

Stumpf, R.P., Holderied, K., Sinclair, M., 2003. Determination of water depth with high-resolution satellite imagery over variable bottom types. Limnol. Oceanogr. 48, 547–556. http://dx.doi.org/10.4319/lo.2003.48.1_part_2.0547.

Thornton, E.B., Guza, R.T., 1982. Energy saturation and phase speeds measured on a natural beach. J. Geophys. Res. 87 (C12), 9499–9508. http://dx.doi.org/10.1029/JC087iC12p09499.

Tissier, M., Bonneton, P., Almar, R., Castelle, B., Bonneton, N., Nahon, A., 2011. Field measurements and non-linear prediction of wave celerity in the surf zone. Eur. J. Mech. B Fluids 30 (6), 635–641. http://dx.doi.org/10.1016/j.euromechflu.2010.11.003.

Vousdoukas, M.I., Kirupakaramoorthy, T., Oumeraci, H., de la Torre, M., Wübbold, F., Wagner, B., Schimmels, S., 2014. The role of combined laser scanning and video techniques in monitoring wave-by-wave swash zone processes. Coast. Eng. 83, 150–165. http://dx.doi.org/10.1016/j.coastaleng.2013.10.013.

Vrbancich, J., Lieff, W., Hacker, J., 2011. Demonstration of two portable scanning LiDAR systems flown at low-altitude for Investigating Coastal sea surface topography. Remote. Sens. 3 (9), 1983–2001. http://dx.doi.org/10.3390/rs3091983.

Yoo, J., Fritz, H.M., Haas, K.A., Work, P.A., Barnes, C.F., 2011. Depth inversion in the surf zone with inclusion of wave nonlinearity using video-derived celerity. J. Waterw. Port Coast. Ocean. Eng. 137 (2), 95–106. http://dx.doi.org/10.1061/(ASCE)WW.1943-5460.0000068.